A high-affinity, dimeric inhibitor of PSD-95 bivalently interacts with PDZ1-2 and protects against ischemic brain damage

Anders Bach, Bettina H Clausen, Magda Moller, Bente Vestergaard, Celestine N Chi, Adam Round, Pernille L Sorensen, Klaus B Nissen, Jette S Kastrup, Michael Gajhede, Per Jemth, Anders S Kristensen, Patrik Lundström, Kate L Lambertsen and Kristian Stromgaard

Linköping University Post Print

N.B.: When citing this work, cite the original article.

A high-affinity, dimeric inhibitor of PSD-95 bivalently interacts with PDZ1-2 and protects against ischemic brain damage

Anders Bach[a,1], Bettina H. Clausen[b], Magda Møller[a], Bente Vestergaard[a], Celestine N. Chi[c], Adam Round[d], Pernille L. Sørensen[a], Klaus B. Nissen[a], Jette S. Kastrup[a], Michael Gajhede[a], Per Jemth[c], Anders S. Kristensen[a], Patrik Lundström[e], Kate L. Lambertsen[b], Kristian Strømgaard[a,1]

[a]Department of Medicinal Chemistry, University of Copenhagen, DK-2100 Copenhagen, Denmark. [b]Department of Neurobiology Research, Institute of Molecular Medicine, University of Southern Denmark, DK-5000 Odense, Denmark. [c]Department of Medical Biochemistry and Microbiology, Uppsala University, BMC, SE-75123 Uppsala, Sweden. [d]European Molecular Biology Laboratory, Grenoble Outstation, 38042 Grenoble, France. [e]Department of Physics, Chemistry and Biology, Division of Molecular Biotechnology, Linköping University, SE-58183, Linköping, Sweden.

[1]To whom correspondence should be addressed: anba@farma.ku.dk or krst@farma.ku.dk (tel.: +45 35336114)

Classification: Biological Sciences (Biochemistry)

Abstract

Inhibition of the ternary protein complex of the synaptic scaffolding protein postsynaptic density protein-95 (PSD-95), neuronal nitric oxide synthase (nNOS), and the *N*-methyl-D-aspartate (NMDA) receptor is a potential strategy for treating ischemic brain damage, but high-affinity inhibitors are lacking. Here we report the design and synthesis of a novel dimeric inhibitor, Tat-*N*PEG4(IETDV)$_2$ (Tat-*N*-dimer), which binds the tandem PDZ1-2 domain of PSD-95 with an unprecedented high affinity of 4.6 nM, and displays extensive protease-resistance as evaluated *in vitro* by stability-measurements in human blood plasma. X-ray crystallography, NMR and small-angle X-ray scattering (SAXS) deduced a true bivalent interaction between dimeric inhibitor and PDZ1-2, and also provided a dynamic model of the conformational changes of PDZ1-2 induced by the dimeric inhibitor. A single intravenous injection of Tat-*N*-dimer (3 nmol/g) to mice subjected to focal cerebral ischemia reduces infarct volume with 40% and restores motor functions. Thus, Tat-*N*-dimer is a highly efficacious neuroprotective agent with therapeutic potential in stroke.

Protein-protein interactions mediated by postsynaptic density protein-95 (PSD-95)/Discs-large/ZO-1 (PDZ) domains are important for intracellular signaling events, and several PDZ domains are potential drug targets for neuronal diseases and cancer (1, 2). The postsynaptic scaffolding protein PSD-95 simultaneously binds the *N*-methyl-D-aspartate (NMDA)-type of ionotropic glutamate receptors and the enzyme neuronal nitric oxide synthase (nNOS) through its PDZ1 and PDZ2 domains (3). Activation of the NMDA receptor causes influx of Ca^{2+}, which activates nNOS thereby leading to nitric oxide generation (4), a key facilitator of glutamate-mediated excitotoxicity (5, 6). Ligands that bind to the first two PDZ domains of PSD-95 inhibit the formation of the ternary nNOS/PSD-95/NMDA receptor complex and uncouple the harmful production of nitric oxide from NMDA receptor activity (Fig. 1*A*). As PSD-95 inhibition does not affect ion-flux (7) or pro-survival signaling pathways (8) mediated by the NMDA receptor, it is believed that compounds targeting PDZ1 and PDZ2 of PSD-95 can provide an efficient and safe treatment of ischemic brain damage (9), where excitotoxicity is known to dominate in the acute post-stroke period, as well as other NMDA receptor-related disorders such as chronic pain and Alzheimer's disease (10-14).

The shallow and elongated binding pocket of PDZ domains generally favor binding of peptides or peptide analogues and so far no drug-like small-molecule inhibitors of PDZ domains with affinities below 5 µM have been identified (15). Accordingly, the most advanced PSD-95 inhibitor is a 20-mer peptide, Tat-NR2B9c (7, 8, 16), composed of 9 amino acids corresponding to the C-terminal of the GluN2B subunit of the NMDA receptor, fused to the HIV-1 Tat peptide (17). This peptide have shown promising effects against ischemic brain damage in rats (7, 8, 16), and is currently investigated in clinical trials (18). However, Tat-NR2B9c suffers from low affinity to PDZ1-2 of PSD-95 (19), which might limit its biological effectiveness and clinical potential. Here we present novel dimeric inhibitors that evade these shortcomings, by exploiting that PSD-95 possesses two neighboring PDZ domains (Fig. 1*A*), and show up to 1,000 fold improved affinity compared to Tat-NR2B9c as well as improved blood plasma stability. Our dimeric inhibitors permeate the blood-brain barrier and demonstrate enhanced neuroprotection in mice relative to Tat-NR2B9c. Biophysical studies demonstrate that the dimeric design results in a bivalent binding mode, where the two ligand moieties bind PDZ1

and PDZ2 simultaneously, hence explaining the high affinity and improved *in vivo* neuroprotection.
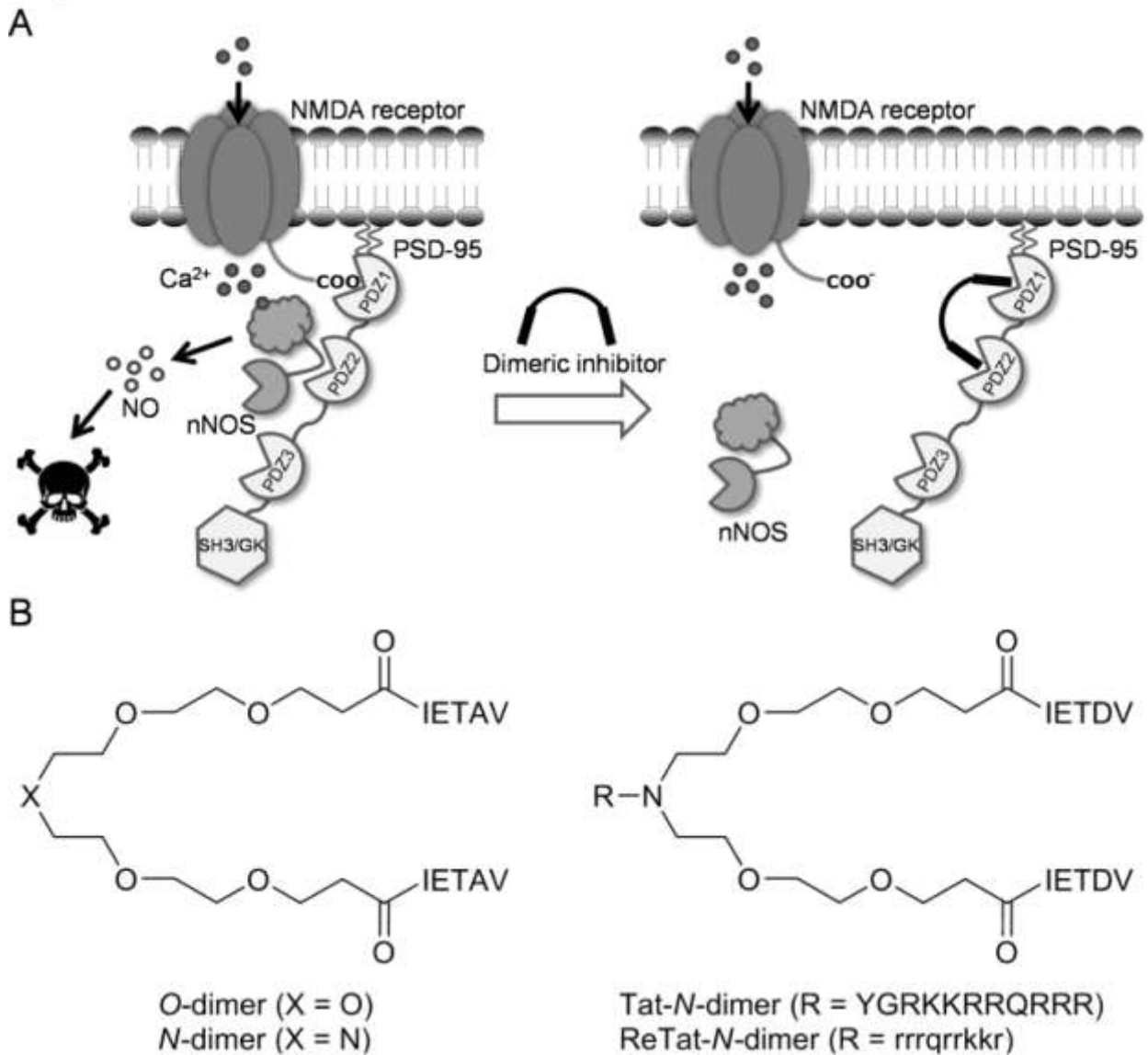
Fig. 1. Dimeric PSD-95 inhibitors. (*A*) PSD-95 inhibitors targeting PDZ1-2 of PSD-95 block the formation of the ternary nNOS/PSD-95/NMDA receptor complex and uncouple the link between NMDA receptor activity and nitric oxide production, whereby neuroprotection against excitotoxicity is achieved. (*B*) Structures of *O*-dimer and *N*-dimer; and Tat-*N*PEG4(IETDV)$_2$ and Retroinverso-D-Tat-*N*PEG4(IETDV)$_2$, designated Tat-*N*-dimer and ReTat-*N*-dimer, respectively. Capital letters indicate L-amino acids, except for ´N´ (nitrogen), ´O´ (oxygen), ´X´ (N or O), and ´R´ (Tat or ReTat sequence), and lower case letters indicate D-amino acids.

Results

Design and activity of novel dimeric inhibitors

We have previously demonstrated that the five C-terminal amino acids of GluN2B are sufficient for maintaining wild-type binding affinity towards the individual PDZ1 (K_i = 14 µM) and PDZ2 (K_i = 3 µM) domains (19). Thus, by linking two pentapeptides (IETAV) with a mono-disperse polyethylene glycol (PEG) linker of optimal length, a high-affinity dimeric ligand, PEG4(IETAV)$_2$ (*O*-dimer) (Fig. 1*B*), is obtained with K_d (mean ± SEM) of 9.8 ± 1.6 nM towards tandem PDZ1-2 of PSD-95 (20, 21). We here redesigned the PEG linker, and synthesized a novel PEG-based linker, termed *N*PEG (Scheme S1*A*), where the central oxygen of the PEG4 linker is replaced by nitrogen, which upon linkage with two IETAV moieties provides *N*PEG4(IETAV)$_2$ (*N*-dimer) (Fig. 1*B*). In order to improve permeability across the blood-brain barrier, we attached the cell-penetrating peptide sequences, Tat and its inverse D-amino acid-containing version Retroinverso-D-Tat (22), to the linker nitrogen, and used IETDV as ligand moiety, which is more selective than IETAV towards PDZ1 and PDZ2 over PDZ3 (20). This resulted in dimeric ligands Tat-*N*PEG4(IETDV)$_2$ (Tat-*N*-dimer) and Retroinverso-D-Tat-*N*PEG4(IETDV)$_2$ (ReTat-*N*-dimer) (Fig. 1*B*, Scheme S1*B*, and Fig. S1).

For *in vitro* affinity evaluation we developed a revised fluorescence polarization assay, where we prepared fluorescently (5-FAM, ***F***) labeled *N*-dimer (***F***-*N*-dimer, Fig. S1) and used it as a high-affinity probe (K_d; mean ± SEM: 7.8 ± 0.1 nM). This allowed us to determine accurate K_i values for high-affinity ligands in a simple and fast format (20, 23). Tat-*N*-dimer and ReTat-*N*-dimer displayed affinities (K_i; mean ± SEM) of 4.6 ± 0.3 and 5.1 ± 0.4 nM, respectively, against PDZ1-2 of PSD-95, whereas *N*-dimer bound PDZ1-2 with an affinity (K_i; mean ± SEM) of 9.3 ± 1 nM (Fig. 2*A*). Tat-*N*-dimer is thereby by far the most potent PDZ domain inhibitor described (15, 24-26), and provides a 1,000-fold increase in affinity relative to monomeric Tat-NR2B9c (K_i; mean ± SEM: 4,600 ± 300 nM, Fig. 2*A*).

A general concern of peptide-based compounds is their susceptibility to enzymatic cleavage in biological fluids and tissues. Monomeric pentapeptide IETDV and Tat-NR2B9c showed half-lives ($T_{1/2}$; mean ± SEM) of 37 ± 6 and 1,100 ± 300 minutes in human blood plasma *in vitro*, respectively, while Tat-*N*-dimer had a $T_{1/2}$ (mean ± SEM) of 4,900 ± 100 minutes (Fig. 2*A*), thus having >100 fold improved stability compared to IETDV. Hence, the combination of

5

dimerization and attachment of cell-penetrating peptides has a striking positive effect on protease stability. Further, no detectable degradation was observed for ReTat-*N*-dimer within the period of measurements, demonstrating the effect of incorporating D-amino acids into the cell-penetrating peptide sequence (Fig. 2*A*).
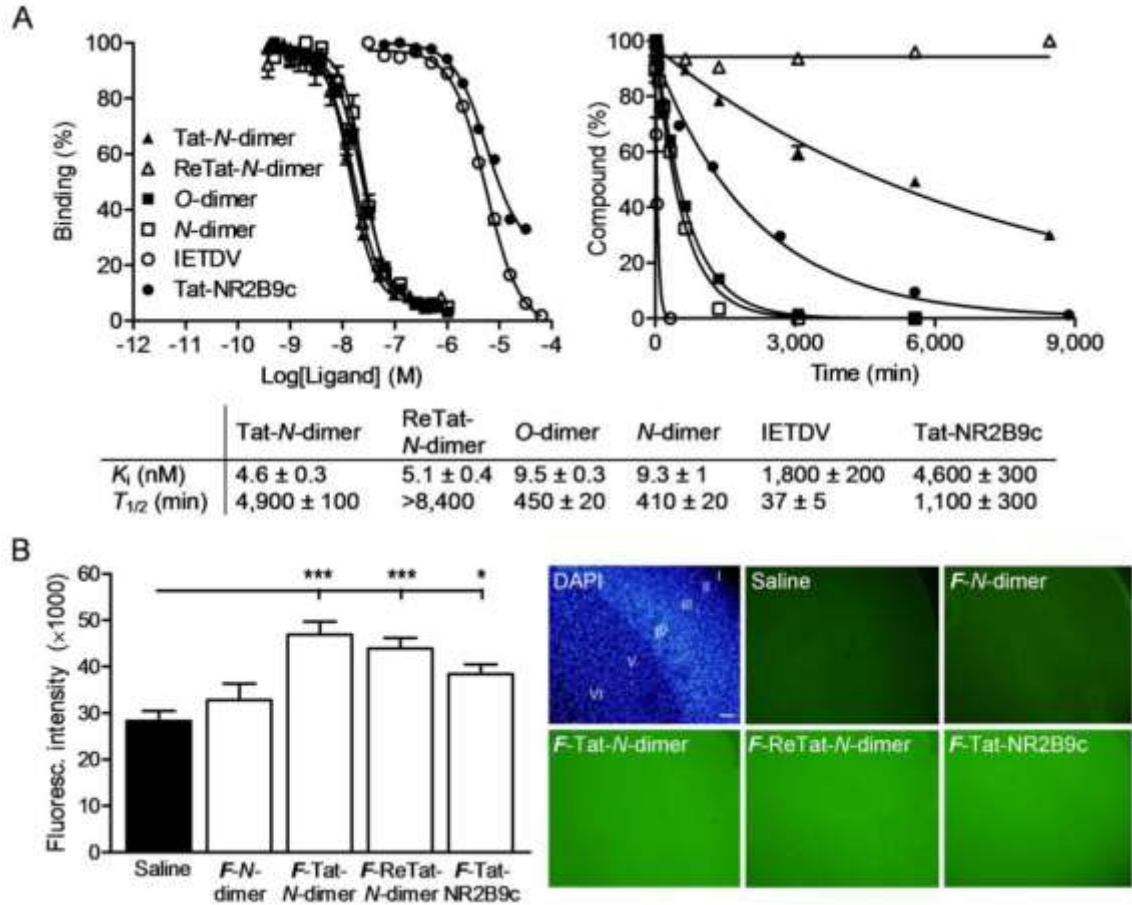

	Tat-*N*-dimer	ReTat-*N*-dimer	O-dimer	*N*-dimer	IETDV	Tat-NR2B9c
K_i (nM)	4.6 ± 0.3	5.1 ± 0.4	9.5 ± 0.3	9.3 ± 1	1,800 ± 200	4,600 ± 300
$T_{1/2}$ (min)	4,900 ± 100	>8,400	450 ± 20	410 ± 20	37 ± 5	1,100 ± 300

Fig. 2. Affinity, stability and blood-brain barrier permeability. (*A*) Affinity towards PDZ1-2 of PSD-95 for Tat-*N*-dimer, ReTat-*N*-dimer and Tat-NR2B9c as measured by fluorescence polarization (left); and stability in human blood plasma *in vitro* at 37 °C (right). Data are shown as mean ± SEM, N ≥ 3. Mean affinity inhibition constants (K_i) and half-lives ($T_{1/2}$) are shown in the table below. (*B*) Blood-brain barrier permeability of fluorescent analogues in non-manipulated mice. The bar graph shows the mean fluorescence intensity of coronal brain slices of mice treated with ***F***-*N*-dimer (p = 0.22), ***F***-Tat-*N*-dimer (p = 0.0002), ***F***-ReTat-*N*-dimer (p = 0.0008), ***F***-Tat-NR2B9c (p = 0.011) compared to saline two hours after intravenous injection. Representative pictures of the cortical area of the coronal brain slices are shown. A nuclei-DAPI staining (blue) is included for anatomical reference showing layers I-VI of the frontal cortex. ***F*** = 5-FAM; Data are presented as mean ± SEM; */**/***: p<0.05/0.01/0.001 (non-parametric Mann-Whitney). Scale bar: 100 µm.

6

To test the effect of introducing cell-penetrating peptides on the permeability of the blood-brain barrier, the ligands were labeled with 5-FAM (**F**) and injected intravenously in mice (3 nmol/g). Fluorescence microscopy of coronal brain slices revealed that **F**-Tat-*N*-dimer, **F**-ReTat-*N*-dimer, and **F**-Tat-NR2B9c resulted in a strong uniform fluorescence throughout the brain including layer I-VI of the frontal cortex, as compared to sections from **F**-*N*-dimer and saline treated mice (Fig. 2*B*). Thus blood-brain barrier permeability of the dimeric compounds is obtained by introduction of Tat or ReTat (7).

Dimeric inhibitor bivalently interacts with PDZ1-2, leading to a flexible and extended conformation

Previous kinetic and mutational studies have suggested that a dimeric ligand binds to PDZ1-2 in a two-step process, where initial binding to either of the two PDZ domains is followed by an intramolecular step leading to the bidentate complex (21). In order to provide structural evidence for such a genuine dimeric binding mode, where both PDZ domains are occupied by the peptide moieties from the same dimeric ligand, and to gain insight into the molecular details and dynamics of the binding mode, we elucidated the molecular mode of action of our dimeric ligands. First, the domain orientation of the two PDZ domains in apo PDZ1-2 was determined by X-ray crystallography, which, however, showed that the two binding sites face approximately 180° away from each other in an extended conformation that cannot accommodate the dimeric ligands (Fig. 3*A* and Table S1). Therefore, we prepared a labeled dimeric ligand, [^{15}N, ^{13}C]-*O*-dimer, and subjected it to structural in solution NMR studies. In an HSQC spectrum of the dimeric, symmetrical ligand alone, five peaks were observed, whereas ten different peaks appeared when the ligand was incubated with PDZ1-2 (Fig. 3*B*). From secondary structural calculations based on the chemical shifts for the bound and unbound labeled dimeric ligand, we observed that the unbound ligand exhibits random coil character, while the bound ligand adopts a β-stranded structure (Fig. 3*C*). Thus, the two peptide moieties of the dimeric ligand face different protein environments (PDZ1 and PDZ2) and β-strand character of the peptide moieties is imposed by binding to PDZ1-2 similar to a canonical PDZ-peptide binding mode (27).

The dynamic properties of PDZ1-2 upon ligand binding were revealed by calculating correlation times for molecular tumbling of PDZ1 and PDZ2 in PDZ1-2 in complex with *O*-

dimer based on R_1 and R_2 relaxation rate measurements. This gave correlation times slightly larger and with less deviation (14.6 and 13.6 ns for PDZ1 and PDZ2, respectively, Table S2) than those reported for PDZ1-2 bound to monomeric ligand (14.4 and 12.5 ns) (28), but very different from values for unbound PDZ1-2 (18.3 and 18.2 ns, Table S2). Hence, these values suggest that the interdomain motion of PDZ1-2 is only slightly more restricted in complex with dimeric ligand than with a monomeric ligand, while unbound PDZ1-2 is essentially rigid.
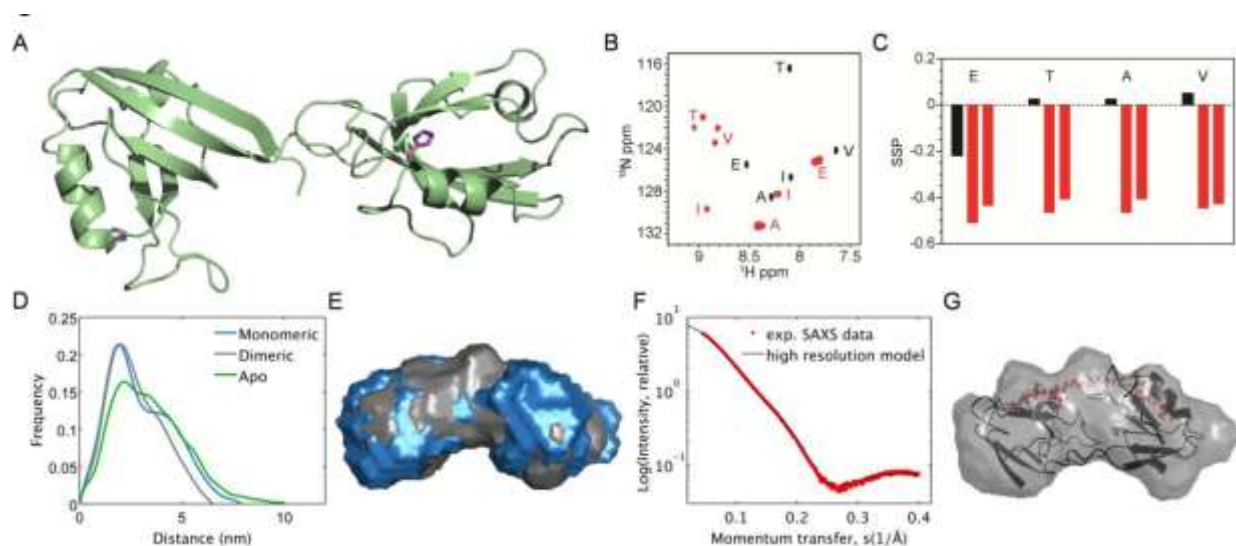

Fig. 3. Biophysical characterization of PDZ1-2 from PSD-95 and interaction with inhibitors. (*A*) X-ray crystal structure of apo PDZ1-2 (PDB 3ZRT). Two conserved histidine residues (His130 and His225) important for ligand binding and with a relative distance of 42 Å are highlighted. (*B*) ^{1}H-^{15}N correlation spectra of free [^{15}N, ^{13}C]-*O*-dimer (black contours) and [^{15}N, ^{13}C]-*O*-dimer in complex with PDZ1-2 from PSD-95 (red contours). Amino acid assignment is indicated with capital letters. (*C*) Secondary structure propensities (SSP) of unbound [^{15}N, ^{13}C]-*O*-dimer (black bars) and [^{15}N, ^{13}C]-*O*-dimer bound to PDZ1-2 (red bars) as calculated using the program SSP. A value of one indicates a fully formed α-helix and a value of minus one indicates a fully extended structure whereas a value close to zero is indicative of a random coil. (*D*) Pair distance distribution functions derived from Fourier transformation of the SAXS data presented as the relative occurrence of distances (arbitrary scale) against distances in nm. Data from apo PDZ1-2 (green), PDZ1-2 with monomeric ligand (IETAV) (blue), and PDZ1-2 with dimeric ligand (*O*-dimer) (gray) are shown. The average radius of the two PDZ domains is visible as the first major peak (around 2 nm, PDZ1 and PDZ2 have similar radii), and the distance between the center of mass of PDZ1 and PDZ2 is seen as the second peak. (*E*) Surface representations of PDZ1-2 bound to IETAV (blue) or *O*-dimer (gray), showing that PDZ1-2 adopts a more compact conformation when bound to *O*-dimer compared to IETAV. (*F*) Comparison of the high-resolution *O*-dimer/PDZ1-2 model (black) and the experimental SAXS scattering data (red). $X = 1.15$. (*G*) High-resolution model of PDZ1-2 in complex with *O*-dimer.

To further examine the structural changes in PDZ1-2 upon ligand binding, we performed small angle X-ray scattering (SAXS) studies of PDZ1-2. In apo PDZ1-2, a distinct distance of approximately 3.3 nm is observed (Fig. 3*D*), which likely represents the average distance between PDZ1 and PDZ2 when no ligand is bound to the protein. Interestingly, this distance increases upon binding of *O*-dimer (3.6 nm) and even more upon binding of monomeric ligand IETAV (3.9 nm) (Fig. 3*D* and Table S3). This demonstrates that the closed and compact apo PDZ1-2 becomes more extended when the dimeric ligand binds, and even further extended by the monomeric ligand, as visualized by low-resolution *ab initio* models of the *O*-dimer and IETAV PDZ1-2 complexes (Fig. 3*E*). The two PDZ domains can be located within the *O*-dimer/PDZ1-2 *ab initio* model, which differs from other reported PDZ1-2 conformations (Fig. S2), by energy minimization so that *O*-dimer bivalently binds to PDZ1-2, and the peptide moieties of *O*-dimer interact with each PDZ domain in a canonical manner (Fig. 3*F-G*). In conclusion, the SAXS and NMR studies unambiguously demonstrate that the dimeric ligand spans the distance between individual domains, interacts with the PDZ domains in a canonical binding mode, and induces a conformation of PDZ1-2 that is more extended and flexible than unbound PDZ1-2, but more compact and restricted compared to PDZ1-2 in complex with monomeric ligand.

Tat-*N*-dimer protects against ischemic brain damage in mice

Encouraged by the remarkably high affinity of Tat-*N*-dimer towards PSD-95 and its stability in blood plasma, we examined Tat-*N*-dimer as a potential *in vivo* active neuroprotectant. We tested Tat-*N*-dimer as well as Tat-NR2B9c and *O*-dimer in the permanent middle cerebral artery occlusion (pMCAO) model of focal ischemia in adult mice (29). Compounds were injected (3 nmol/g) once, intravenously, 30 minutes after the pMCAO insult, followed by a 6 hour post-surgical survival period (Fig. 4*A*). Animals receiving Tat-*N*-dimer showed a 40% reduction in ischemic tissue damage compared to saline-treated animals (p = 0.0081) (Fig. 4*B*), whereas treatment with *O*-dimer gave no neuroprotective effect (p = 0.62, N = 19), indicating the necessity for introducing cell-penetrating peptides into the dimeric ligands to obtain effects *in vivo*. Treatment with Tat-NR2B9c did not provide a statistically significant reduction in infarct volumes (Fig. 4*B*) (p = 0.22), although we verified by immunofluorescence employing a primary

anti-Tat antibody that both Tat-*N*-dimer and Tat-NR2B9c were located inside neuron-like cells (30) 6 hours after pMCAO (Fig. 4*C*).
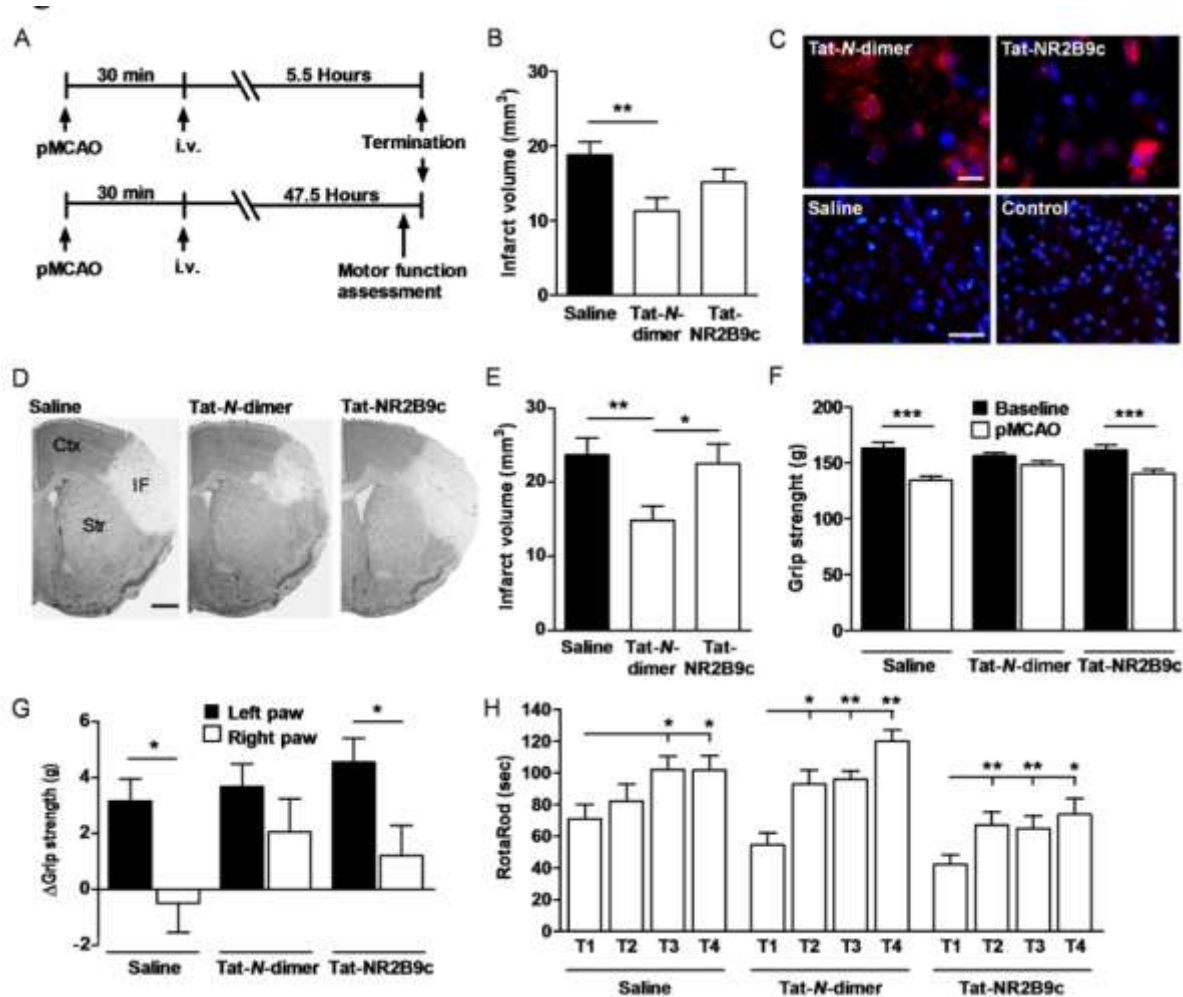

Fig. 4. Neuroprotection of Tat-*N*-dimer, 6 and 48 hours after pMCAO in mice. (*A*) Compounds were administered 30 minutes post-surgery, followed by a survival period of 5.5 or 47.5 hours. (*B*) Mean infarct volumes 6 hours after pMCAO of mice treated with Tat-*N*-dimer (N = 17), Saline (N = 16), or Tat-NR2B9c (N = 18). (*C*) Immunofluorescent staining of cells containing Tat-based compounds, Tat-*N*-dimer and Tat-NR2B9c, 6 hours after pMCAO, co-labelled with nuclei-DAPI staining (blue). Sections from both saline-injected mice, and Tat-*N*-dimer treated mice where the primary antibody was substituted with isotype control, were devoid of signal. Scale bar: 20 µm (upper), 40 µm (lower). (*D*) Toluidine blue staining showing the ischemic brain damage 48 hours after pMCAO. IF: Infarct; Ctx: Cortex; Str: Striatum. Scale bar: 1 mm. (*E-G*) Motor function assessment of mice with 48 hours post-surgical survival. (*E*) Mean infarct volumes 48 hours after pMCAO of mice treated with Tat-*N*-dimer (N = 17), Saline (N = 16), or Tat-NR2B9c (N = 17). (*F*) Mean total grip strength of both front paws before (baseline) and after pMCAO. P-values: <0.0001 (Saline), 0.13 (Tat-*N*-dimer), 0.0011 (Tat-NR2B9c). (*G*) Ischemia induced grip strength asymmetry in the front paws. P-values: 0.014 (Saline), 0.11 (Tat-*N*-dimer), 0.013 (Tat-NR2B9c). (*H*) Rotarod performance test over four trials (T1-T4). A learning component is observed along the trials in all groups, but treatment with Tat-*N*-dimer gave a more pronounced improvement (cf. T2) compared to saline, and increased endurance compared to Tat-NR2B9c (see text). (*B, E-H*) Data are shown as mean ± SEM; */**/***: p<0.05/0.01/0.001; (*B* and *E*) Nonparametric Mann-Whitney test; (*F-G*) Paired Student's *t* test; (*H*) Wilcoxon matched pairs test.

10

To evaluate prolonged effects of Tat-*N*-dimer, we performed the pMCAO experiment with a 48 hour post-surgical survival period (Fig. 4*A*) and observed a 37% reduction in infarct size compared to saline-treated mice (p = 0.0042) (Fig. 4*D-E*). Again, Tat-NR2B9c gave no statistically significant infarct reductions (p = 0.89) (Fig. 4*D-E*), but treating animals with ReTat-*N*-dimer under similar conditions led to a 34% reduction in infarct volumes (p = 0.0094) (Fig. S3). Body temperature, weight and blood gas parameters were monitored during the pMCAO experiment and no differences were observed among the treated groups (Fig. S4 and Table S4).

Focal cerebral ischemia induced by pMCAO in mice affects cortical brain areas controlling the contralateral front- and hind-limb including the paws (31). Thus, we included behavioral tests that challenged the motor function of mice subjected to pMCAO. In accordance with reduced infarct volumes, the total grip strength of both paws was unaffected for animals treated with Tat-*N*-dimer, but reduced for those given saline or Tat-NR2B9c (Fig. 4*F*). Similarly, there was no difference in grip strength between the right and left front paw for Tat-*N*-dimer-treated animals in contrast to treatment with saline or Tat-NR2B9c (Fig. 4*G*). Finally, in the rotarod performance test we observed that Tat-*N*-dimer resulted in a more pronounced short-term learning skill improvement than saline-treated mice (Fig. 4*H*), and the total time spent on the rod was significantly longer (83.5 ± 4.1 seconds; average of trial 1-4 ± SEM) than for mice treated with Tat-NR2B9c (65.7 ± 3.7 seconds; average of trial 1-4 ± SEM) (P<0.001). The effects on motor control of ReTat-*N*-dimer were similar to those observed for Tat-*N*-dimer (Fig. S3).

Discussion

PSD-95 is a potential target for protection against ischemic brain damage (9), and recent studies demonstrate promising effects of PSD-95 inhibitors in animal models of pain (10-12) and Alzheimer's disease (13). Despite this intriguing role of PSD-95, there is a lack of inhibitors against PSD-95, and PDZ domains in general, with reasonably affinity and *in vivo* activity, which impede the possibilities for exploiting PDZ domains as drug targets. Here we have advanced the concept of dimeric inhibitors against the tandem PDZ1-2 domain of PSD-95 in order to develop potent *in vivo* active ligands. Previously, two decapeptides targeting PDZ1 and PDZ2 have been linked via disulphide bonds from *N*-terminal cysteine residues, which resulted in 5-20 fold increase in affinity relative to the monomeric ligand (24), and a related design with peptide

sequences of 15 amino acids resulted in a similar 8-25 fold increase in affinity (25). In the present work, the dimeric ligands provide a remarkable 400-fold increase in affinity compared to the monomeric peptide. This has been achieved by optimizing peptide length and sequence as well as the linker length, and in particular, by the essential modification of changing the PEG linker into *N*PEG, which allows cell-penetrating peptides to be attached to the dimeric structure without compromising binding affinities. Tat-*N*-dimer displays an unprecedented high affinity for any PDZ domain-mediated interaction with a K_i value of 4.6 nM, which is a 1,000-fold improvement compared to Tat-NR2B9c. In addition, our design provides a solution to the inherent problem of peptides being degraded in biological fluids, as Tat-*N*-dimer, and in particular ReTat-*N*-dimer, demonstrates greatly enhanced stability in blood plasma. Moreover, both compounds cross the blood-brain barrier in mice and demonstrate significant *in vivo* neuroprotective properties, hence Tat-*N*-dimer reduces ischemic stroke damage in mice with 40% and significantly improves motor functions.

We observe that the high-affinity compounds, Tat-*N*-dimer and ReTat-*N*-dimer, are more efficient *in vivo* neuroprotectants in the mouse pMCAO model compared to the low-affinity monomeric inhibitor Tat-NR2B9c, which did not show statistical significant infarct reductions. Tat-NR2B9c has previously shown promising effects in both transient and permanent focal ischemic stroke models in rats (7, 8, 16), but these studies cannot be directly compared to the current mouse study due to experimental differences (32). It is, however, noteworthy that under the same conditions and dosages in mice, we see superior activity of the dimeric inhibitors relative to Tat-NR2B9c. Whether this represents generally improved neuroprotective properties across species and types of ischemic stroke models needs confirmation by future studies. In addition, the permanent MCAO model induces a smaller ischemic penumbra than the transient MCAO model in the acute phase after stroke (<4-6 hours after arterial occlusion) where neuroprotection is believed to be achievable (33, 34). As a result of this, large percentages of rescued tissues are harder to obtain in the permanent model. Hence, a 40% infarct reduction in a permanent model as a result of a single post-stroke administration of Tat-*N*-dimer is highly promising, and its relevance is underlined by the concomitant improvement in motor functions and persistency after 48 hours (32).

To elucidate the mode of action at the molecular level of the dimeric ligands we applied a combination of X-ray crystallography, NMR and SAXS. Previous NMR studies suggest that apo PDZ1-2 of PSD-95 adopts a closed and rigid conformation (24), in agreement with the C-shaped arrangement of full-length PSD-95 observed by electron microscopy (35), and that the interdomain mobility of PDZ1 and PDZ2 is increased upon monomeric peptide binding, leading to a flexible and more extended peptide-bound conformation (28). Based on these observations, it was suggested that this increased conformational freedom of PDZ1-2 upon ligand binding provides extra conformational entropy, which facilitates ligand binding (28). This intriguing model initially seemed contradictory to the fact that our dimeric ligands display such a large affinity-increase compared to monomeric compounds, as one would expect dimeric ligands to rigidify PDZ1-2 and hence lead to a large entropy penalty. However, our NMR and SAXS studies provide unambiguous evidence for apo PDZ1-2 to be compact and rigid compared to when PDZ1-2 is bound to monomeric compound where it is more extended and flexible. Moreover, these studies demonstrate that dimeric ligand, although it does make PDZ1-2 more compact relative to monomeric ligand, still facilitates interdomain flexibility of PDZ1-2 to about the same extent as monomeric ligand, thus potentially allowing the conformational entropy of PDZ1-2 to be increased. This could also explain the pronounced difference in affinity of the different types of dimeric inhibitors of PSD-95. We have used very flexible *N*PEG or PEG-based linkers to dimerize the peptide ligands, whereas other dimeric ligands are less flexible (24, 25) and might therefore be paying a higher entropic penalty, leading to decreased affinity, due to rigidifying PDZ1-2.

PDZ domains generally work as structural and functional modules in neuronal scaffolding and adaptor proteins, and frequently appear as tandem supramodular domains, similar to PDZ1-2 of PSD-95 (36). The dimeric design presented here is in principle applicable to any protein containing a tandem PDZ domain. Thus, by linking appropriate peptide ligands using the *N*PEG linker and attachment of cell-penetrating peptides, the methodology demonstrated here is a versatile and straightforward way of generating *in vivo* active tool compounds and potential therapeutics for proteins containing tandem PDZ domains and even for other bi-modular targets.

In summary, we have designed and synthesized dimeric ligands that are highly efficient inhibitors of the tandem PDZ1-2 domain of the scaffolding protein PSD-95. Tat-*N*-dimer binds

PDZ1-2 with unprecedented high affinity, displays extensive stability in blood plasma, crosses the blood-brain barrier, reduces ischemic stroke damage in mice with 40% and improves motor functions. Using biophysical methods, we have provided unequivocal evidence for a bivalent binding mechanism and characterized the conformational changes upon ligand binding. Tat-*N*-dimer is at present the most efficient PSD-95 inhibitor described, and could become a valuable pharmacological tool for studying PSD-95-related biology and for paving the way for dimeric PSD-95 inhibitors as drug candidates.

Experimental Procedures

Complete descriptions of ligand synthesis and characterization, protein purification, affinity and stability *in vitro* assays, X-ray crystallography, NMR, SAXS, modeling, and *in vivo* experiments are found in *SI Experimental Procedures.*

Author contributions

A.B., B.H.C., B.V., C.N.C., M.G., P.J., A.S.K., K.L.L. and K.S. designed research; A.B., B.H.C., M.M., C.N.C., A.R., P.L.S., K.B.N., P.L., and K.L.L performed research; A.B., B.H.C., B.V., J.S.K., M.G., P.L., K.L.L, and K.S. analyzed data; and A.B. and K.S. wrote the paper.

Accession code

Coordinates and structure factors for the PDZ1-2 crystal structure have been deposited in the Protein Data Bank under accession code 3ZRT.

Competing financial interests

The authors declare no competing financial interests.

References

1. Blazer LL, Neubig RR (2009) Small molecule protein-protein interaction inhibitors as cns therapeutic agents: Current progress and future hurdles. *Neuropsychopharmacology* 34:126-141.

2. Dev KK (2004) Making protein interactions druggable: Targeting pdz domains. *Nat Rev Drug Discov* 3:1047-1056.

3. Christopherson KS, Hillier BJ, Lim WA, Bredt DS (1999) PSD-95 assembles a ternary complex with the *N*-methyl-D-aspartic acid receptor and a bivalent neuronal NO synthase PDZ domain. *J Biol Chem* 274:27467-27473.

4. Sattler R, et al. (1999) Specific coupling of NMDA receptor activation to nitric oxide neurotoxicity by PSD-95 protein. *Science* 284:1845-1848.

5. Dawson VL, et al. (1991) Nitric oxide mediates glutamate neurotoxicity in primary cortical cultures. *Proc Natl Acad Sci U S A* 88:6368-6371.

6. Huang Z, et al. (1994) Effects of cerebral ischemia in mice deficient in neuronal nitric oxide synthase. *Science* 265:1883-1885.

7. Aarts M, et al. (2002) Treatment of ischemic brain damage by perturbing NMDA receptor-PSD-95 protein interactions. *Science* 298:846-850.

8. Soriano FX, et al. (2008) Specific targeting of pro-death NMDA receptor signals with differing reliance on the NR2B PDZ ligand. *J Neurosci* 28:10696-10710.

9. Tymianski M (2011) Emerging mechanisms of disrupted cellular signaling in brain ischemia. *Nat Neurosci* 14:1369-1373.

10. Tao F, Su Q, Johns RA (2008) Cell-permeable peptide Tat-PSD-95 PDZ2 inhibits chronic inflammatory pain behaviors in mice. *Mol Ther* 16:1776-1782.

11. LeBlanc BW, et al. A cyclic peptide targeted against PSD-95 blocks central sensitization and attenuates thermal hyperalgesia. *Neuroscience* 167:490-500.

12. D'Mello R, et al. (2011) Perturbing PSD-95 interactions with NR2B-subtype receptors attenuates spinal nociceptive plasticity and neuropathic pain. *Mol Ther* 19:1780-1792.

13. Ittner LM, et al. (2010) Dendritic function of tau mediates amyloid-β toxicity in Alzheimer's disease mouse models. *Cell* 142:387-397.

14. Gardoni F (2008) MAGUK proteins: New targets for pharmacological intervention in the glutamatergic synapse. *Eur J Pharmacol* 585:147-152.

15. Bach A, et al. (2011) Cell-permeable and plasma-stable peptidomimetic inhibitors of the postsynaptic density-95/*N*-methyl-D-aspartate receptor interaction. *J Med Chem* 54:1333-1346.

16. Sun HS, et al. (2008) Effectiveness of PSD95 inhibitors in permanent and transient focal ischemia in the rat. *Stroke* 39:2544-2553.

17. Schwarze SR, Ho A, Vocero-Akbani A, Dowdy SF (1999) In vivo protein transduction: Delivery of a biologically active protein into the mouse. *Science* 285:1569-1572.

18. Tat-NR2B9c is found under the name NA-1 at www.clinicaltrials.gov.

19. Bach A, et al. (2008) Modified peptides as potent inhibitors of the postsynaptic density-95/*N*-methyl-D-aspartate receptor interaction. *J Med Chem* 51:6450-6459.

20. Bach A, et al. (2009) Design and synthesis of highly potent and plasma-stable dimeric inhibitors of the PSD-95/NMDA receptor interaction. *Angew. Chem. Int. Ed.* 48:9685–9689.

21. Chi CN, et al. (2010) Deciphering the kinetic binding mechanism of dimeric ligands using a potent plasma-stable dimeric inhibitor of postsynaptic density protein-95 as an example. *J Biol Chem* 285:28252-28260.

22. Wender PA, et al. (2000) The design, synthesis, and evaluation of molecules that enable or enhance cellular uptake: Peptoid molecular transporters. *Proc Natl Acad Sci U S A* 97:13003-13008.

23. Huang X (2003) Fluorescence polarization competition assay: The range of resolvable inhibitor potency is limited by the affinity of the fluorescent ligand. *J Biomol Screen* 8:34-38.

24. Long JF, et al. (2003) Supramodular structure and synergistic target binding of the N-terminal tandem PDZ domains of PSD-95. *J Mol Biol* 327:203-214.

25. Sainlos M, et al. (2011) Biomimetic divalent ligands for the acute disruption of synaptic AMPAR stabilization. *Nat Chem Biol* 7:81-91.

26. Paduch M, et al. (2007) Bivalent peptides as models for multimeric targets of PDZ domains. *Chembiochem.* 8:443-452.

27. Doyle DA, et al. (1996) Crystal structures of a complexed and peptide-free membrane protein-binding domain: Molecular basis of peptide recognition by PDZ. *Cell* 85:1067-1076.

28. Wang W, et al. (2009) Creating conformational entropy by increasing interdomain mobility in ligand binding regulation: A revisit to N-terminal tandem PDZ domains of PSD-95. *J Am Chem Soc* 131:787-796.

29. Lambertsen KL, et al. (2009) Microglia protect neurons against ischemia by synthesis of tumor necrosis factor. *J Neurosci* 29:1319-1330.

30. Lyck L, Krøigård T, Finsen B (2007) Unbiased cell quantification reveals a continued increase in the number of neocortical neurones during early post-natal development in mice. *Eur J Neurosci* 26:1749-1764.

31. Pronichev I, Lenkov D (1998) Functional mapping of the motor cortex of the white mouse by a microstimulation method. *Neurosci Behav Physiol* 28:80-85.

32. Ginsberg MD (2008) Neuroprotection for ischemic stroke: Past, present and future. *Neuropharmacology* 55:363-389.

33. Hata R, et al. (2000) Dynamics of regional brain metabolism and gene expression after middle cerebral artery occlusion in mice. *J Cereb Blood Flow Metab* 20:306-315.

34. Hata R, et al. (2000) Evolution of brain infarction after transient focal cerebral ischemia in mice. *J Cereb Blood Flow Metab* 20:937-946.

35. Nakagawa T, et al. (2004) Quaternary structure, protein dynamics, and synaptic function of SAP97 controlled by l27 domain interactions. *Neuron* 44:453-467.

36. Feng W, Zhang M (2009) Organization and dynamics of PDZ-domain-related supramodules in the postsynaptic density. *Nat Rev Neurosci* 10:87-99.

A high-affinity, dimeric inhibitor of PSD-95 bivalently interacts with PDZ1-2 and protects against ischemic brain damage

Anders Bach[a,1], Bettina H. Clausen[b], Magda Møller[a], Bente Vestergaard[a], Celestine N. Chi[c], Adam Round[d], Pernille L. Sørensen[a], Klaus B. Nissen[a], Jette S. Kastrup[a], Michael Gajhede[a], Per Jemth[c], Anders S. Kristensen[a], Patrik Lundström[e], Kate L. Lambertsen[b], Kristian Strømgaard[a,1]

Supporting Information

Experimental Procedures

Chemistry (General).

Amino acids, preloaded Wang resins, 2-chlorotrityl chloride resin, and monodisperse PEG4-diacid were purchased from IRIS Biotech (Marktredwitz, Germany). 5-Carboxyfluorescein (5-FAM) was purchased from Anaspec (San Jose, CA, USA), and building blocks for synthesizing the Ns-*N*PEG4 linker were obtained from Biomatrik Inc. (Jiaxing, China). ^{15}N,^{13}C-labeled Fmoc-protected amino acids were purchased from Cambridge Isotope Laboratories, Inc. (Andover, MA, USA). Preparative reverse phase high-performance liquid chromatography (RP-HPLC) was performed on a Agilent 1200 system using a C18 reverse phase column (Zorbax 300 SB-C18, 21.2 mm × 250 mm) with a linear gradient of the binary solvent system of H$_2$O/MeCN/trifluoroacetic acid (TFA) (A, 95/5/0.1, and B, 5/95/0.1) with a flow rate of 20 mL/min. Analytical HPLC was performed on an Agilent 1100 system with a C18 reverse phase column (Zorbax 300 SB-C18 column, 4.6 mm × 150 mm), flow rate of 1 mL/min, and a linear gradient of the binary solvent system of H$_2$O/MeCN/TFA (A, 95/5/0.1, and B, 5/95/0.1). Mass spectra were obtained with an Agilent 6410 Triple Quadrupole Mass Spectrometer instrument using electron spray ionization (ESI) coupled to an Agilent 1200 HPLC system (ESI-LC/MS) with a C18 reverse phase column (Zorbax Eclipse XBD-C18, 4.6 mm × 50 mm), autosampler and diode array detector using a linear gradient of the binary solvent system of H$_2$O/MeCN/formic acid (A, 95/5/0.1, and B, 5/95/0.086) with a flow rate of 1 mL/min. During ESI-LC/MS analysis, evaporative light scattering (ELS) traces were obtained with a Sedere Sedex 85 Light Scattering Detector. High-resolution mass spectra (HRMS) were obtained using an electron spray ionization (ESI) and Micromass Q-Tof 2 instrument.

Peptide synthesis.

Peptide sequences were synthesized manually by Fmoc-based solid phase peptide chemistry using preloaded Fmoc-Val-Wang-resin (0.6-0.7 mmol/g, 100-200 mesh), *O*-(benzotriazol-1-yl)-*N,N,N′,N′*-tetramethyluronium hexafluorophosphate (HBTU)/ diisopropylethylamine (DIPEA) for couplings, and dry DMF as solvent. Each coupling was carried out for 40 min with resin/Fmoc-amino acid/HBTU/DIPEA (1:4:3.9:8), and was qualitatively evaluated by the ninhydrin test. Fmoc-deprotection was carried out in 20% piperidine in DMF for 5 min, followed by DMF wash and a second piperidine/DMF treatment for 15 min.

Purification and Characterization.

Compounds were obtained as TFA salts by treating the resin-bound products with TFA/triisopropylsilane/H_2O (90/5/5) for 2 hours followed by filtration, evaporation *in vacuo*, precipitation with cold ether, lyophilization, and purification with preparative RP-HPLC. For *in vivo* experiments, compounds were prepared as HCl salts by incubating the TFA salts of the compounds with ice cold aq. HCl (50 mM) for 20 min followed by lyophilization (1). All final compounds were characterized for purity (>98%) (UV218) by analytical HPLC and for purity (>98%) (UV218, ELSD) and molecular mass by ESI-LC/MS.

Synthesis of the Ns-*N*PEG4 linker [10-((2-nitrophenyl)sulfonyl)-4,7,13,16-tetraoxa-10-azanonadecane-1,19-dioic acid].

2-Chlorotrityl chloride resin (3 mmol, 1.90 g) was washed (DMF, 15 flow washes, each of 10 mL), swelled (DMF, 15 mL, 20 min), drained, and treated with Fmoc-NH-PEG$_2$-CH$_2$CH$_2$COOH (2 mmol, 800 mg, **1**, Scheme S1*A*) in dry DMF (8 mL) and DIPEA (10 mmol, 1.75 mL). After shaking for 60 min, MeOH (1 mL, 25 mmol) was added, and shaking was continued for 5 min. The loaded resin was drained and flow-washed with DMF (15 flow washes, each of 10 mL), and the Fmoc group was de-protected with 20% piperidine in DMF (15 mL) for 5 min and 15 min with a DMF flow-wash in between, followed by a DMF and THF flow-wash. The resin was swelled in DIPEA (12 mmol, 2.1 mL) and THF (8 mL) for 15 min, and *ortho*-nitrobenzenesulfonyl chloride (NsCl, 8 mmol, 1.78 g) in DCM (5 mL) was added slowly while gently stirring the resin. After addition of NsCl, the resin was shaken for 4 hours, drained and flow-washed consecutively with THF, MeOH, DCM, and THF. The resin (1 eq., 2 mmol) was treated with triphenylphosphine (PPh$_3$, 10 mmol, 2625 mg) in THF (5 mL) and HO-PEG$_2$-CH$_2$CH$_2$COO*t*Bu (10 mmol, 2.34 g, **2**, Scheme S1*A*) in THF (5 mL) under nitrogen. Diisopropyl azodicarboxylate (DIAD, 10 mmol, 2.02 g, 1.97 mL) was added dropwise followed by shaking for 1 hour. The resin was flow-washed with THF and DCM, dried *in vacuo* and treated with TFA/triisopropylsilane/H_2O (90/5/5, 20 mL) for 2.5 hours. The TFA-mixture was collected and the resin was washed with TFA and DCM before the combined TFA/DCM fractions were evaporated and co-evaporated with ether (2 × 30 mL). The resulting material was dissolved in water/MeCN (75/25, 100 mL) and lyophilized to provide Ns-*N*PEG4 linker (**3**, Scheme S1*A*) as

an orange oil, which was used without further purification. Yield: 80%. Purity: >98%. m/z (ESI) 540.1 (22%), 523.1 (M^++H, 100), 505.1 (11), 433.0 (7.3), 365.2 (7.4).

Synthesis of *N*-dimer, Tat-*N*-dimer, and ReTat-*N*-dimer.

The Ns-*N*PEG4 linker (**3**, 0.1 eq., 0.025 mmol) was pre-activated with HBTU (0.2 eq, 0.05 mmol) and DIPEA (0.4 eq, 0.1 mmol) and added to Fmoc-deprotected Wang-resin-bound IETDV (1 eq, 0.25 mmol) in DMF (4 mL) followed by 45 min of shaking and a DMF flow-wash. This was repeated 5 times to obtain ~90% dimerization efficiency (LC/MS) (Scheme S1*B*). The *ortho*-nitrobenzenesulfonyl (Ns) group was readily removed by adding 1,8-Diazabicyclo[5.4.0]undec-7-ene (DBU, 0.5 mmol) in DMF (2 mL) directly followed by mercaptoethanol (0.5 mmol) in DMF (2 mL) and shaking for 30 min. After a flow-wash in DMF, the mercaptoethanol/DBU treatment was repeated, and the resin flow-washed consecutively with DMF, DCM, MeOH and DCM. For Tat- and ReTat-*N*-dimer the first amino acid from the sequence (L- or D-Arg, respectively) was coupled to the nitrogen by six consecutive couplings of Fmoc-Arg(Pbf)-OH (Scheme S1*B*). For each coupling, Fmoc-Arg(Pbf)-OH (0.5 mmol) was activated by *O*-(7-azabenzotriazol-1-yl)-*N,N,N′,N′*-tetramethyluronium hexafluorophosphate (HATU) in DMF (2 mL, 0.244M) and collidine (132 µL), before addition to the drained resin. After 45 min of shaking and a DMF flow-wash, the coupling and DMF wash was repeated 5 times. Fmoc was removed with 20% piperidine in DMF and the remaining Tat- or Retroinverso-D-Tat sequence synthesized as described in the ´peptide synthesis´ section. HRMS (ESI+) calcd. for $C_{126}H_{226}N_{43}O_{41}$ $[M + 5H]^+$, 599.7391; found, m/z 599.7245 (Tat-*N*-dimer). HRMS (ESI+) calcd. for $C_{115}H_{212}N_{41}O_{38}$ $[M + 3H]^+$, 925.5317; found, m/z 925.5207 (ReTat-*N*-dimer).

Synthesis of *F*-Tat-*N*-dimer, *F*-ReTat-*N*-dimer, *F*-Tat-NR2B9c and *F*-*N*-dimer.

Fluorescent ligands were prepared by coupling 5-FAM (*F*) to the *N*-terminal amino group of the final and Fmoc-deprotected Tat-*N*-dimer, ReTat-*N*-dimer, or Tat-NR2B9c, while bound to the resin, to provide *F*-Tat-*N*-dimer, *F*-ReTat-*N*-dimer, and *F*-Tat-NR2B9c, respectively. Likewise, 5-FAM was coupled to Ns-deprotected, resin-bound *N*-dimer to furnish *F*-*N*-dimer. 5-FAM was coupled with *N*-sites-resin/5-FAM/HATU/collidine (1:2:2:3) in a total of 2 mL DMF at a 0.07 mmol scale (molar of *N*PEG-linker). For *F*-Tat-*N*-dimer, *F*-ReTat-*N*-dimer, and *F*-Tat-NR2B9c,

coupling time was 6 hours. For **F**-*N*-dimer, 5-FAM was coupled by two consecutive couplings of 6 and 16 hours, respectively.

Synthesis of [^{15}N, ^{13}C]-*O*-dimer.

The following uniformly labeled amino acids were used for the synthesis of [^{15}N, ^{13}C]- *O*-dimer: Fmoc-L-Val-[^{13}C$_5$,^{15}N]-OH, Fmoc-L-Ala-[^{13}C$_3$,^{15}N]-OH, Fmoc-L-Thr-[^{13}C$_4$,^{15}N]-(*t*Bu)-OH, Fmoc-L-Glu-[^{13}C$_5$,^{15}N]-(*t*Bu)-OH, and Fmoc-L-Ile-[^{13}C$_6$,^{15}N]-OH. Fmoc-L-Val-[^{13}C$_5$,^{15}N]-OH (0.125 mmol, 43 mg) was dissolved in DMF (1.5 mL) and loaded to a portion of 2-chlorotrityl chloride resin (0.1875 mmol, 119 mg) that had been swelled in DMF (2 mL) for 20 min and drained. DIPEA (0.625 mmol, 109 µL) was added and shaking was continued for 60 min. MeOH (100 µL) was added, shaking continued for 15 min, and the resin washed with DMF. Fmoc was removed with piperidine/DMF and labeled IETAV was further synthesized using resin/Fmoc-amino acid/HATU/collidine (1:2:2:3) in DMF (1 mL) for 40 min. After the final Fmoc-removal, the resin was washed with DMF and DCM, dried *in vacuo* and used further to prepare [^{15}N, ^{13}C]-*O*-dimer by the on-resin dimerization method used for the synthesis of *O*-dimer, as described previously (2).

Expression and purification of PDZ1-2 of PSD-95.

For X-ray and NMR studies, PDZ1-2 (residues 61-249, referring to the residue numbers in the human full-length PSD95α without exon 4b, Uniprot accession number P78352) was produced as previously described (3). Uniformly [^{15}N] labeled PDZ1-2 for NMR was expressed by growing the bacterial culture in M9 minimal media supplemented with [^{15}N]-NH$_4$Cl as the sole nitrogen source. For fluorescence polarization and SAXS experiments, the cDNA coding for the same PSD-95 PDZ1-2 sequence (residue 61-249) and an additional *N*-terminal His-tag sequence (MHHHHHHHRS)* was cloned into the pRSET A vector (Invitrogen, Carlsbad, CA). PDZ1-2 was expressed in *E. coli* (BL21-DE3 pLysS) and purified from bacterial lysates by a nickel (II)-charged column followed by gel-filtration as described previously (3). The His-tag was removed by digestion of the purified PDZ1-2 protein with the exoprotease, TAGZyme DAPase enzyme (Qiagen, Hilden, Germany), following the manufacturer´s protocol. After 48 hours the protein precipitated and was re-dissolved in 6 M GnHCl (2 mL) and dialyzed twice in phosphate buffer (20 mM NaH$_2$PO$_4$, 150 mM NaCl, pH 7.5; 1 L) for three and 15 hours, respectively, to ensure

maximal refolding of the protein. PDZ1-2 was obtained by a "reverse purification" on the HisTrap using Tris-buffer (50 mM Tris-HCl, pH 7.5), and lyophilization of PDZ1-2-containing fractions, reconstitution in 6 M GnHCl and dialysis in 20 mM Tris-HCl, pH 7.5 (1 × 3 hours and 1 × 15 hours, 2 × 1 L) provided pure PDZ1-2 as evaluated by SDS-PAGE and ESI-LC/MS. Protein concentrations were calculated from molar absorption coefficients determined from amino acids analysis (Alphalyze, Odense, Denmark).

* PDZ1-2 protein sequence with the His-tag (removed during purification method) indicated in parentheses:

(MHHHHHHH)RSMEYEEITLERGNSGLGFSIAGGTDNPHIGDDPSIFITKIIPGGAAAQDGR LRVNDSILFVNEVDVREVTHSAAVEALKEAGSIVRLYVMRRKPPAEKVMEIKLIKGPKG LGFSIAGGVGNQHIPGDNSIYVTKIIEGGAAHKDGRLQIGDKILAVNSVGLEDVMHEDAV AALKNTYDVVYLKVAKPSNA

Fluorescence polarization assay.

The affinity between the fluorescent probe, *F*-*N*-dimer, and PDZ1-2 was determined using a saturation binding methodology. Increasing concentrations of PDZ1-2 were added to a fixed concentration (0.5 nM) of the probe, and the assay was performed with TBS buffer (150 mM NaCl, 10 mM Tris, pH 7.4) in black, low protein-binding 384-well plates (Corning Life Sciences, NY, USA). After incubation for 10 min at room temperature, the fluorescence polarization of the samples was measured on a Safire2 plate-reader (Tecan, Männedorf, Switzerland) at excitation/emission wavelengths of 470/525 nm. Graphical plots of the fluorescence polarization values as a function of PDZ1-2 concentrations were fitted to the equation $Y = B_{max} \times X/(K_d + X)$, where B_{max} is the maximal fluorescence polarization value, X is the total PDZ1-2 concentration, Y is the fluorescence polarization value, and K_d is the dissociation constant. The affinities between non-fluorescent compounds and PDZ1-2 were determined by heterologous competition, where increasing concentrations of ligand were added to a fixed concentration of probe (0.5 nM) and PDZ1-2 (7.8 nM) under identical conditions as for saturation binding. Fluorescence polarization values were fitted to the equation $Y = Bottom + (Top - Bottom)/[1 + (10^{(X-LogIC50*nH)})]$, where X is the logarithmic value of total ligand concentration, IC_{50} is the total ligand concentration that produces a half-maximal inhibition, nH is the Hill slope, *Bottom* is the fluorescence polarization value at saturating conditions, and *Top*

is the fluorescence polarization value in absence of compound. The resulting IC_{50} values were converted to competition inhibition constants, K_i values, as described (4). All values reported are the average of at least three individual experiments. Ligand stock concentrations were verified by amino acid analysis.

Human blood plasma stability assay.

Compounds (30 µL of a 2.5 mM water stock) were dissolved in human blood plasma (270 µL, normal human plasma, pooled, 3H Biomedical, Uppsala, Sweden) to a concentration of 0.25 mM and incubated at 37 °C. Aliquots (30 µL) were quenched at sequential time points by addition of 5% w/v aqueous trichloroacetic acid (60 µL), vortexed and incubated for 15 min at 4 °C followed by centrifugation at 18,000 g for 2 min. The supernatants were analyzed by analytical RP-HPLC (UV_{218}) to quantify compounds relative to time zero, and also evaluated qualitatively by ESI-LC/MS to identify the compound (m/z) in the sample. Procaine (positive control) and procainamide (negative control) were investigated at 50 µM. Ligand recoveries following the TCA precipitation procedure were between 85-95%.

X-ray crystallography of PDZ1-2 of PSD-95.

For X-ray studies, PDZ1-2 preparations with intact His-tag were used as previously described (3). Crystals were obtained as thin rods using the hanging drop vapour diffusion method and a 250 µL reservoir solution containing 0.1 M sodium acetate trihydrate pH 6.0, 2.0 M sodium formate and 5% PEG 4000 (drop size: 1 µL protein sample + 1 µL reservoir solution). The crystallographic data are summarized in Table S1. Diffraction data were obtained on microfocus beamline ID23-2, ESRF, Grenoble France. Due to radiation damage, a full dataset (44 frames) was assembled from four data collections on the same crystal but translated to different regions. The data were indexed and scaled to 3.4 Å resolution using MOSFLM (5) and SCALA (6) within CCP4 (7, 8). The protein crystallized in the space group $P4_12_12$ with four molecules in the asymmetric unit. The structure was solved using the molecular replacement program PHASER (9) within CCP4 with a search model generated by the program BALBES (10). The generated model was based on the X-ray structure of SAP-102-PDZ1 (PDB 2I1N). The amino acid sequence of the search models had been changed to that of PSD-95 PDZ2 and side chains of long flexible residues as Lys, Arg and Glu were truncated. Flexible loops and the C- and N-terminal

ends were also truncated. From the first search using PHASER, four domains were identified. Visual examination showed that these four domains were well-defined by the electron density, and well-defined electron density was also observed in the unmodeled regions of the linkers and loops. The identified domains were fixed when searching for additional domains in the following molecular replacement runs. Also, the percentage cut-off used for selection in the rotation search was lowered to 65, 60 and 55%, respectively. In this manner, solutions for seven domains in total were identified. The last domain (PDZ1 of molecule D) was also localized in the molecular replacement search, but the electron density in several areas around this was very poor compared to the other domains. In the final molecular replacement solution clear difference electron density could be observed in PDZ1-PDZ2 linker regions.

The structure was refined to R_{work}/R_{free} values of 21.9/26.4% and validated using program PHENIX (11). Before building the unmodeled regions, the structure was refined using a rigid-body refinement scheme. The R_{free}-value was high (40.8%) after this refinement, but as the structure was corrected and the unmodeled regions were built using program COOT (12), R_{free} decreased rapidly. After the rigid-body refinement, the refinement of the structure was continued using combined TLS, B-group and NCS. B-group was selected over B-individual due to the medium resolution of the data and the NCS restraints were important, as the structure was otherwise over-fitted to the data. Between each refinement step every residue was examined in the 2Fo-Fc and Fo-Fc maps and if necessary adjusted. In the initial refinements (up to step 5), PDZ1 and the linker region between PDZ1 and PDZ2 of molecule D were not built due to poor electron density around this domain. Examination of the electron density map (2Fo-Fc) and the omit map (Fo-Fc) in this region revealed well-defined electron density in some areas. Modeling of the linker and parts of the domain resulted in a decrease in R_{free} by ca. 2%. Later, the number of residues to be included in the domain was revised, and refinements revealed that deleting residues with poorly defined side chains did not affect the R_{free}-value. A slight decrease (0.5%) in the difference between the R-values suggested that the structure was less over-fitted to the data in the final structure (step 6) compared to step 5, possibly as a result of the deleted residues in PDZ1 of molecule D between step 5 and 6. In the final structure, the linker of molecule D and the three β-strands: βA, βD and βF of PDZ1 were included in the structure. βA, βD and βF form an antiparallel β-sheet; thus, these residues have several contacts to each other. Polar contacts

from these β-strands to other domains in the crystal were also observed, which was not the case for the rest of the domain if it were built. These contacts might induce more order in this part of the domain, which might explain why it is possible to identify βA, βD and βF of molecule D.

NMR studies of PDZ1-2 of PSD-95.

NMR samples comprised a 3.5 mM solution of $[^{15}N,^{13}C]$-O-dimer alone or 2.2 mM solution of the same compound saturated with unlabeled PDZ1-2 in 50 mM potassium phosphate, pH 7.5 in 9/1 H_2O/D_2O. All experiments were recorded at a static magnetic field corresponding to a proton Larmor frequency of 600 MHz and the temperature was 25 °C and 30 °C for assignment and relaxation experiments, respectively. HNCA, HN(CA)CO and HSQC experiments were recorded to assign the backbone of the peptide moieties of the free compound. For the bound compound HNCACB, HN(CA)CO and HSQC experiments were recorded for assignment purposes. ^{15}N R_1 and $R_{1\rho}$ relaxation rates as well as the $\{^1H\}$-^{15}N NOE were measured for 2.8 mM $[^{15}N]$-PDZ1-2 saturated with unlabeled O-dimer using previously described pulse sequences (13, 14). Sample conditions were as above. For the R_1 experiment, the following relaxation delays were used: 0.01, 0.05, 0.1, 0.2, 0.3, 0.4, 0.5, 0.6, 0.7, 0.8, 0.9, 1.0 sec. Uncertainties in peak intensities were estimated from five duplicate data points. The $R_{1\rho}$ experiment was recorded with a spinlock field of 1661 Hz and the radiofrequency carrier positioned at 119 ppm and relaxation delays of 0.004, 0.008, 0.012, 0.016, 0.0,02, 0.024, 0.03, 0.036, 0.04, 0.05, 0.055, 0.06 sec. Five duplicate data points were recorded for estimation of uncertainties in peak volumes. $\{^1H\}$-^{15}N NOE was recorded by taking the ratio of experiments recorded with and without saturating the protons. The total recycle delay for both experiments was 12 sec and the experiment without the saturation pulses was duplicated for estimation of uncertainties. The relaxation experiments were repeated for a 0.4 mM sample of unbound $[^{15}N]$-PDZ1-2, i.e. without the presence of ligand. All NMR data were processed using NMRpipe (15) and visualized using Sparky (Goddard and Kneller, University of California at San Francisco). Assignments for the bound and unbound forms of PDZ1-2 were obtained by transferring the assignments from PDZ1-2/cypin (16) and free PDZ1-2 (17), respectively. Since a different compound was used in this study and since sample conditions were different, only slightly more than half of the assignments could be transferred with confidence. The remaining peaks in the spectra were not analyzed. Peaks were integrated and volumes converted into relaxation rates using the in house program PINT (Ahlner

A., Carlsson M., Jonsson B.H. and Lundström P., Linköping University; available upon request). The same program was used to convert $R_{1\rho}$ relaxation rates into R_2 relaxation rates. The correlation time for molecular tumbling was estimated from the R_2/R_1 ratio, excluding residues with NOE<0.65 (18). The secondary structure for free and bound [^{15}N, ^{13}C]-O-dimer was calculated with the program SSP (19).

SAXS studies of PDZ1-2 of PSD-95.

Measurements were done over a range of protein concentrations (0.25-7.1 mg/mL). To ensure full saturation, a 5:1 mixture ratio of ligand:protein were used at all protein concentrations. SAXS data were collected at beamline ID14-3 at ESRF, Grenoble, France (20). The automated sample loader was used, applying a continued flow of maximally 40 µL of sample, while applying 10 times 10 seconds of exposures at 8 °C. Individual exposures were radially averaged and compared for potential radiation damage, and those exposures where damage was evident were discarded before averaging. Pure buffer samples were measured before and after the protein samples, and an average of the two data files was used for background subtraction. The primary data reduction was performed using PRIMUS which is part of the ATSAS suite (21). The molecular mass of the protein complex in the sample was estimated via internal calibration with a bovine serum albumin sample. Radius of gyration was estimated by the Guinier approximation implemented in PRIMUS, and the fourier transformation was calculated using the program GNOM (22). The program CRYSOL was applied for comparison to the known high-resolution structures (23). The *ab initio* modeling program DAMMIF (24), which is a novel faster implementation of the precursor DAMMIN (25), was implemented for generation of the solution model reconstructions. Ten models were calculated in the slow mode, using standard settings. The program DAMAVER (26) was applied to superimpose individual structures, and to evaluate the spatial discrepancy between individual models. The averaged and filtered model (available upon request) was used for the visualization in Fig. 3*E* and Fig. S2. High-resolution structures were optimally oriented for minimization of spatial discrepancy onto the filtered model by applying the program SUPCOMB (27).

High-resolution model of the *O*-dimer/PDZ1-2 complex.

The model of PDZ1-2 in complex with *O*-dimer (Fig. 3*G*) was created by implementing the rigid body modeling program BUNCH, which uses simulated annealing combined with *ab initio* modeling approaches for determining the optimal position of high-resolution protein domains by fitting these against SAXS data (28). The NMR based PDZ1-2 model (17) in complex with pentapeptides (2) was fitted in BUNCH against the experimental SAXS scattering data for PDZ1-2 bound to *O*-dimer. A flexible linker (residue 88-96) was defined between PDZ1 and PDZ2 to allow interdomain mobility. The *O*-dimer was build into the resulting BUNCH recreation model by connecting the pentapeptides with the PEG4 linker, and subsequently, the complex was energy minimized without constraints using the force field OPLS2005 in Macromodel (Version 9.5, Schrödinger, LLC, New York, NY, USA) to create the final high-resolution *O*-dimer/PDZ1-2 model (available upon request). The model was optimally oriented onto the filtered solution structure of PDZ1-2 bound to *O*-dimer using SUPCOMB (Fig. 3*G*), and CRYSOL was applied for comparison of the final high-resolution model and the experimental scattering data giving $X = 1.15$ (Fig. 3*F*).

Mice for *in vivo* studies.

The permanent middle cerebral artery occlusion (pMCAO) study was performed using age-matched, young adult (7-8 weeks), male C57BL/6 mice (Taconic, Denmark). Mice were housed in separate cages under diurnal lighting and given free access to food (1314 Altromin, Brogården, Denmark) and water. Mice acclimatized for 7 days prior to surgery in accordance with guidelines approved by the Danish Animal Ethical Committee (J. no. 2005/561-1068).

Group size and study design.

The extent of the ischemic infarct was measured in two separate randomized, double-blinded, placebo controlled studies: 1) Determination of the neuroprotective effects of *O*-dimer, Tat-*N*-dimer, and Tat-NR2B9c compared to saline, as evaluated 6 hours after pMCAO; and 2) Determination of the neuroprotective effects of Tat-*N*-dimer, ReTat-*N*-dimer, and Tat-NR2B9c compared to saline, as evaluated 48 hours after pMCAO. In the 6 hour survival study, 82 mice were used, of which 4 died due to anesthesia and 8 were found not to have an infarct and was therefore excluded. In the 48 hour survival study, 82 mice were used, 5 died due to anesthesia

11

and 8 were found not to have an infarct and was therefore excluded. For investigation of blood-brain barrier permeability in non-manipulated mice 10 mice were used.

Permanent middle cerebral artery occlusion (pMCAO).

Surgical procedure: Mice were subjected to focal cerebral ischemia by permanent occlusion of the middle cerebral artery (MCA), as previously described (29). Briefly, the animals were anesthetized by subcutaneous injections of 0.18 mL per 10 gram body weight, of a 1:1:2 mixture of Hypnorm^{TM} (fentanyl citrate 0.315 mg/mL and fluanisone 10 mg/mL, VectaPharma Ltd), Midazolam (5 mg/mL, Hameln), and distilled H_2O. The mouse was placed on a 37 ± 0.5 °C heating pad and the eyes coated with ointment (Viscotears; Novartis, Basel, Switzerland). A skin incision was made between the lateral part of the orbit and the external auditory meatus. The superior pole of the parotic gland and the upper part of the temporal muscle were pushed aside after partial resection and a small craniotomy, using a 0.8 mm burr was made directly above the distal branch of the MCA. The dura mater was removed and the MCA electrocoagulated using bipolar forceps (Gimmi, Germany) coupled to an electrosurgical unit (ICC50 from ERBE, Germany). Following occlusion of the artery, the muscle and soft tissue were organized and the skin sutured using a 4-0 nylon suture. For management of post-surgical pain, animals were supplied with Temgesic (0.001 mg/20g buprenorphinum, Reckitt & Coleman, UK) three times with an 8 hour interval starting immediately after surgery. In addition, the mice were injected subcutaneously with 1 ml of isotonic saline before transfer to a 28 °C controlled recovery room.

Compound administration: Compounds were dissolved in isotonic (0.9%) saline (NaCl) to a concentration of 300 µM, and 10 µl per gram body weight was administered intravenously (i.v.) (Dose: 3 nmol/g) as a bolus, into the tail vein, 30 min after surgery. Control mice received an i.v. injection of 0.9% NaCl.

Physiological parameters.

Physiological parameters were carefully monitored prior to and in the acute phase after pMCAO surgery (first critical 6 hours).

Body weight monitoring: The body weight of the mouse was registered during pre-training, before surgery, and at 24 and 48 hours after surgery.

Temperature monitoring: The rectal temperature of the mouse was continuously measured using a thermocoupled probe connected to a Model Bat 12 unit (Physitemp). The temperature was measured prior to and 30 min after pMCAO in addition to 30 min and 2.5 hours after i.v. injection, i.e. 1 and 3 hours after pMCAO.

Blood gas analysis: One sample of venous blood was taken for blood gas analysis of PO_2/PCO_2 electrolytes, glucose, lactate, and hematocrit, 30 min after compound administration (1 hour after pMCAO). A capillary heparin coated tube was inserted along the inner corner of eye and turned until it penetrated the conjunctiva. A sample of blood (150 μl) was collected and stored on ice until gas analysis using the GEM Premier 300 blood gas instrument (Instrumentation Laboratory). Quality controls (QC ContrlIL9) were purchased from IL Sensor Systems.

Behavioral tests.
Mice with 48 hours post-surgical survival were examined using three different behavioral tests in order to detect motor deficits that may not necessarily manifest in the infarct size, thereby providing a more general impression of the animal´s condition (30).

Grip strength: The grip strength meter (BIO-GT-3, BIOSEB) allowed the study of neuromuscular functions in mice by determining the maximum force that is required to make the mouse release its grip. The mouse is allowed to grasp a metal grid and then pulled backwards in the horizontal plane. The force applied to the grid is recorded as the peak tension. Individual (right and left) and total (both) front paw grip strength was measured before (baseline) and after pMCAO. Each mouse was tested in 5 sequential trials and the highest grip strength was recorded as the score (29).

Rotarod performance test: The rotarod (LE 8200, Panlab) is well suited to evaluate motor activity in rodents, experimental compound effects on central nervous system damage, or disease effects on motor coordination, assessed by the time during which the animal remains walking on

a rotating drum. The rotation speed of the rotarod is motorically controlled and accelerates from 0 to 40 rounds per min (rpm) over a time period of 5 min (*31*). Mice were tested in 4 repeating trials with a 20 min interval (resting time). Prior to surgery, mice were pre-trained to stay on the rod for 30 seconds, at 4 rpm.

Termination of the mice and brain tissue processing.

C57BL/6 mice with 6 hour post-surgical survival time were euthanized by cervical dislocation. C57BL/6 mice with 48 hour post-surgical survival were anesthetized with an overdose of pentobarbital (the pharmacy of the Faculty of Life Sciences, University of Copenhagen, Denmark) in order to collect blood and tissue samples. All brains were carefully removed, flash-frozen in gaseous CO_2 and cut into 6 series of 30 µm coronal cryostat sections and stored at -80 °C until further use.

Determination of infarct volume.

Frozen brain sections from each mouse were fixated in 70% ethanol over night at 4 °C. Sections were rehydrated and immersed in a toluidin blue solution (0.01% w/v, Merck, Germany) dissolved in 80 mmol/L $Na_2HPO_4 \times 2H_2O$ and 70 mmol/L citric acid, followed by rinsing three times in H_2O and dehydrated in graded series of alcohol (96–99% ethanol). The sections were cleared in xylene and coverslipped in Depex (BDH Gurr, UK) (32). Sections were used for infarct volumetric analysis using a Computer Assisted Sterological Test (CAST) GRID microscope-system (Olympus, Denmark) and the Cavalieri principle for volume estimation (33, 34). The total volume of the infarct (V_{total}) was calculated using the formula: $V_{total} = \sum P * t * a_{point}$, where $\sum P$ is the total number of points hitting the infarct, t is the mean distance between sections, and a_{point} represents the area per point (33).

Immunofluoresence for Tat$^+$-cells.

To detect cells that have taken up Tat-based compounds, i.e. Tat-*N*-dimer and Tat-NR2B9c, parallel cryostat sections obtained from mice with 6 hours post-surgical survival were fixed in 4% paraformaldehyde (PFA) for 10 min and rinsed 2 × 10 min in 0.05 M Tris-buffered saline (TBS, pH 7.4) followed by pepsin (xx Bettina) digest for 10 min. The sections were rinsed in TBS for 10 min before blocking with 10% fetal calf serum in TBS incl. 0.5% Triton for 30 min,

at room temperature. Next, the sections were blocked for endogenous avidin/biotin (Vector Lab), 10 min each and rinsed 2 × 10 min in TBS. Then sections were incubated with a biotin-conjugated (Serotec) Tat-primary antibody 1:150 (Abcam; mouse monoclonal antibody mapped to amino acids 47-58 [YGRKKRRQRRRA] of HIV-1 Tat) at 4 °C. Following 48 h incubation, the sections were rinsed for 10 min in TBS and incubated with Tritc-conjugated streptavidin (Serotec), diluted 1:200, overnight and briefly counterstained with DAPI (Invitrogen). The isotype control antibody was biotin-conjugated mouse IgG (Dako). The histology results were evaluated by an Olympus DP70 digital camera mounted on an Olympus BX51 microscope connected to a PC with Olympus DP-software.

Blood-brain barrier permeability.

The blood-brain barrier permeability for F-N-dimer, F-Tat-N-dimer, F-ReTat-N-dimer, and F-Tat-NR2B9c was investigated in non-occluded C57BL/6J mice (N = 8), compared with normal saline treated control mice (N = 2).The mice were deeply anesthetized and perfused through the left ventricle 2 hours after i.v. (tail vein) injection of compound, using 10 ml chilled Soerensens phosphate buffer (SB, 25 nM KH_2PO_4, 125 mM Na_2HPO_4, pH 7.4) followed by 20 mL SB containing 4% PFA. The brains were carefully removed and post-fixed in 4% PFA for 1 hour followed by immersion in SB containing 20% sucrose over night. The brains were frozen on gaseous CO_2 and processed into 16 μm coronal cryostat sections. Coronal sections prior to and after the anterior commisure (N = 5) were examined for 5-FAM fluorescence by the use of fluorescence microscopy. The anterior commisure (Bregma: 0.14 mm) was used as a fix point in the brain in order to analyze anatomically identical brain sections. The intensity of the 5-FAM fluorophore was measured semi-quantitatively using a fluorescence microscopy system (Olympus System Microscope model BX-51, Denmark) with a 10× objective (Olympus 10×/0,15 UPlanApo) connected to a high-resolution microscope digital camera (Olympus model DP70), which transferred images to an image-capturing software (Image Pro Plus software). All images were taken in reference to sections from saline treated mice using the same microscope settings and with constant camera exposure time. Fluorescence intensities were quantified using the ImageJ 1.42q software.

Statistical analysis.

Statistical analysis was performed using the Graphpad Instat 5.0 program for Windows (GraphPad software, San Diego, CA, USA). Comparison of mean values of infarction sizes between two groups of mice was done using the non-parametric Mann-Whitney test. Two-tailed, paired Student's *t* test was used to compare grip strength values obtained from the same mouse before and after surgery. Wilcoxon signed-rank test was used on repeated measurements from the same mouse (Rotarod Performance Test). Two-way analysis of variance was used to investigate independent variables (time and weight or temperature). All data are presented as means ± SEM. Statistical significance was accepted for $P<0.05$.

1.   Sani MA, Loudet C, Grobner G, Dufourc EJ (2007) Pro-apoptotic bax-α1 synthesis and evidence for β-sheet to α-helix conformational change as triggered by negatively charged lipid membranes. *J Pept Sci* 13:100-106.

2.   Bach A, et al. (2009) Design and synthesis of highly potent and plasma-stable dimeric inhibitors of the PSD-95/NMDA receptor interaction. *Angew Chem Int Ed* 48:9685–9689.

3.   Bach A, et al. (2008) Modified peptides as potent inhibitors of the postsynaptic density-95/*N*-methyl-D-aspartate receptor interaction. *J Med Chem* 51:6450-6459.

4.   Nikolovska-Coleska Z, et al. (2004) Development and optimization of a binding assay for the XIAP BIR3 domain using fluorescence polarization. *Anal Biochem* 332:261-273.

5.   Leslie AGW (1992) Joint CCP4 + ESF-EAMCB newsletter on protein crystallography 26.

6.   Evans P (2006) Scaling and assessment of data quality. *Acta Crystallogr D Biol Crystallogr* 62:72-82.

7.   Collaborative Computational Project (1994) The CCP4 suite: Programs for protein crystallography. *Acta Crystallogr D Biol Crystallogr* 50:760-763.

8.   Potterton E, Briggs P, Turkenburg M, Dodson E (2003) A graphical user interface to the CCP4 program suite. *Acta Crystallogr D Biol Crystallogr* 59:1131-1137.

9.   McCoy AJ, et al. (2007) Phaser crystallographic software. *J Appl Crystallogr* 40:658-674.

10.   Long F, Vagin AA, Young P, Murshudov GN (2008) Balbes: A molecular-replacement pipeline. *Acta Crystallogr D Biol Crystallogr* 64:125-132.

11.   Adams PD, et al. (2002) Phenix: Building new software for automated crystallographic structure determination. *Acta Crystallogr D Biol Crystallogr* 58:1948-1954.

12.   Emsley P, Cowtan K (2004) Coot: Model-building tools for molecular graphics. *Acta Crystallogr D Biol Crystallogr* 60:2126-2132.

13.   Farrow NA, et al. (1994) Backbone dynamics of a free and a phosphopeptide-complexed Src homology 2 domain studied by ^{15}N NMR relaxation. *Biochemistry* 33:5984-6003.

14.   Korzhnev DM, et al. (2002) An NMR experiment for the accurate measurement of heteronuclear spin-lock relaxation rates. *J Am Chem Soc* 124:10743-10753.

15.   Delaglio F, et al. (1995) NMRPipe: a multidimensional spectral processing system based on unix pipes. *J Biomol NMR* 6:277-293.

16. Wang W, et al. (2009) Creating conformational entropy by increasing interdomain mobility in ligand binding regulation: A revisit to N-terminal tandem PDZ domains of PSD-95. *J Am Chem Soc* 131:787-796.

17. Long JF, et al. (2003) Supramodular structure and synergistic target binding of the N-terminal tandem PDZ domains of PSD-95. *J Mol Biol* 327:203-214.

18. Kay LE, Torchia DA, Bax A (1989) Backbone dynamics of proteins as studied by nitrogen-15 inverse detected heteronuclear NMR spectroscopy: Application to staphylococcal nuclease. *Biochemistry* 28:8972-8979.

19. Marsh JA, Singh VK, Jia Z, Forman-Kay JD (2006) Sensitivity of secondary structure propensities to sequence differences between α- and γ-synuclein: Implications for fibrillation. *Protein Sci* 15:2795-2804.

20. Pernot P, et al. (2010) New beamline dedicated to solution scattering from biological macromolecules at the ESRF. *J Phys Conf Ser* 247:012009.

21. Konarev PV, et al. (2003) Primus: A windows PC-based system for small-angle scattering data analysis. *J Appl Crystallogr* 36:1277-1282.

22. Svergun D (1992) Determination of the regularization parameter in indirect-transform methods using perceptual criteria. *J Appl Crystallogr* 25:495-503.

23. Svergun D, Barberato C, Koch MHJ (1995) CRYSOL - a program to evaluate X-ray solution scattering of biological macromolecules from atomic coordinates. *J Appl Crystallogr* 28:768-773.

24. Franke D, Svergun DI (2009) DAMMIF, a program for rapid ab-initio shape determination in small-angle scattering. *J Appl Crystallogr* 42:342-346.

25. Svergun DI (1999) Restoring low resolution structure of biological macromolecules from solution scattering using simulated annealing. *Biophys J* 76:2879-2886.

26. Volkov VV, Svergun DI (2003) Uniqueness of ab initio shape determination in small-angle scattering. *J Appl Crystallogr* 36:860-864.

27. Kozin MB, Svergun DI (2001) Automated matching of high- and low-resolution structural models. *J Appl Crystallogr* 34:33-41.

28. Petoukhov MV, Svergun DI (2005) Global rigid body modeling of macromolecular complexes against small-angle scattering data. *Biophys J* 89:1237-1250.

29.   Lambertsen KL, et al. (2009) Microglia protect neurons against ischemia by synthesis of tumor necrosis factor. *J Neurosci* 29:1319-1330.

30.   Irwin S (1968) Comprehensive observational assessment: Ia. A systematic, quantitative procedure for assessing the behavioral and physiologic state of the mouse. *Psychopharmacology* 13:222-257.

31.   Brooks SP, Dunnett SB (2009) Tests to assess motor phenotype in mice: A user's guide. *Nat Rev Neurosci* 10:519-529.

32.   Clausen BH, Lambertsen KL, Meldgaard M, Finsen B (2005) A quantitative in situ hybridization and polymerase chain reaction study of microglial-macrophage expression of interleukin-1beta mrna following permanent middle cerebral artery occlusion in mice. *Neuroscience* 132:879-892.

33.   Møller A, et al. (1995) Pharmacological profile and anti-ischemic properties of the Ca^{2+}-channel blocker NS-638. *Neurol Res* 17:353-360.

34.   Gregersen R, Lambertsen K, Finsen B (2000) Microglia and macrophages are the major source of tumor necrosis factor in permanent middle cerebral artery occlusion in mice. *J Cereb Blood Flow Metab* 20:53-65.

35.   Sainlos M, et al. (2011) Biomimetic divalent ligands for the acute disruption of synaptic AMPAR stabilization. *Nat Chem Biol* 7:81-91.

36.   Kleywegt GJ, Jones TA (1996) Phi/psi-chology: Ramachandran revisited. *Structure* 4:1395-1400.

37.   Lee HJ, Zheng JJ (2010) PDZ domains and their binding partners: Structure, specificity, and modification. *Cell Commun Signal* 8:8-25.

Scheme, Figures, Tables
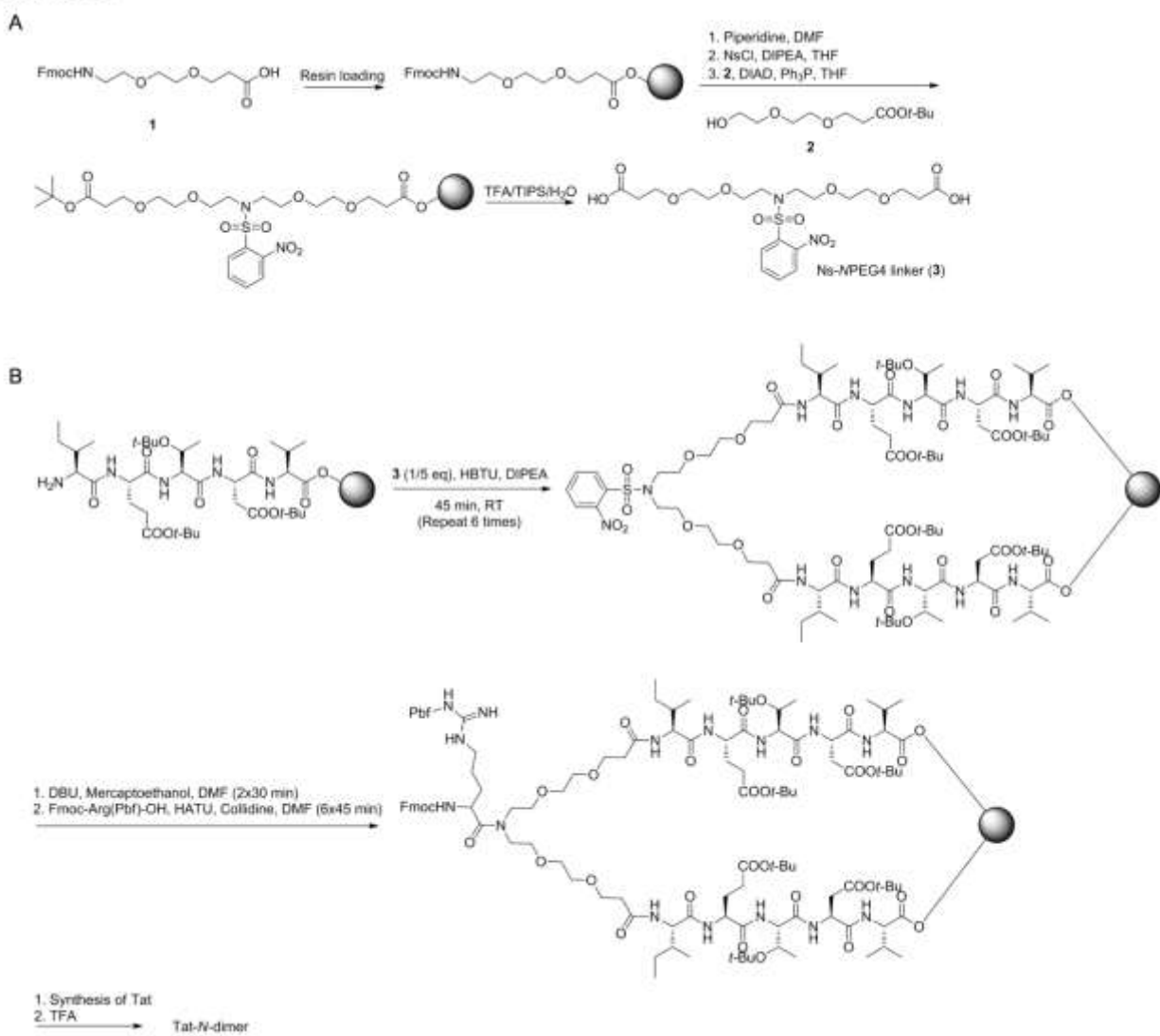
Scheme S1. (*A*) Synthesis of the Ns-*N*PEG4 linker (**3**). (*B*) Synthesis of Tat-*N*-dimer.
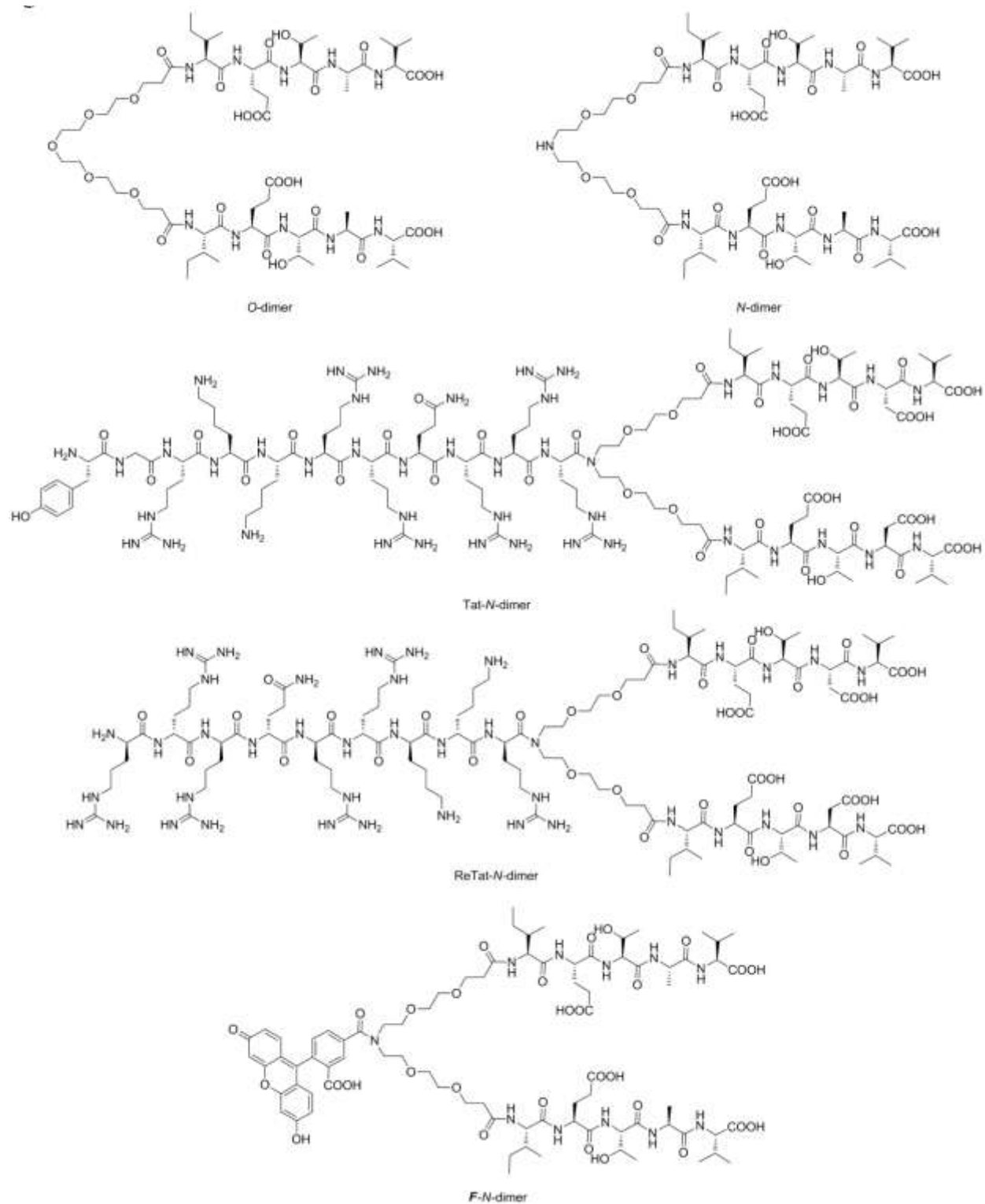
Fig. S1. Structures of *O*-dimer, *N*-dimer, Tat-*N*-dimer, ReTat-*N*-dimer, and ***F***-*N*-dimer. ***F***: 5-FAM.
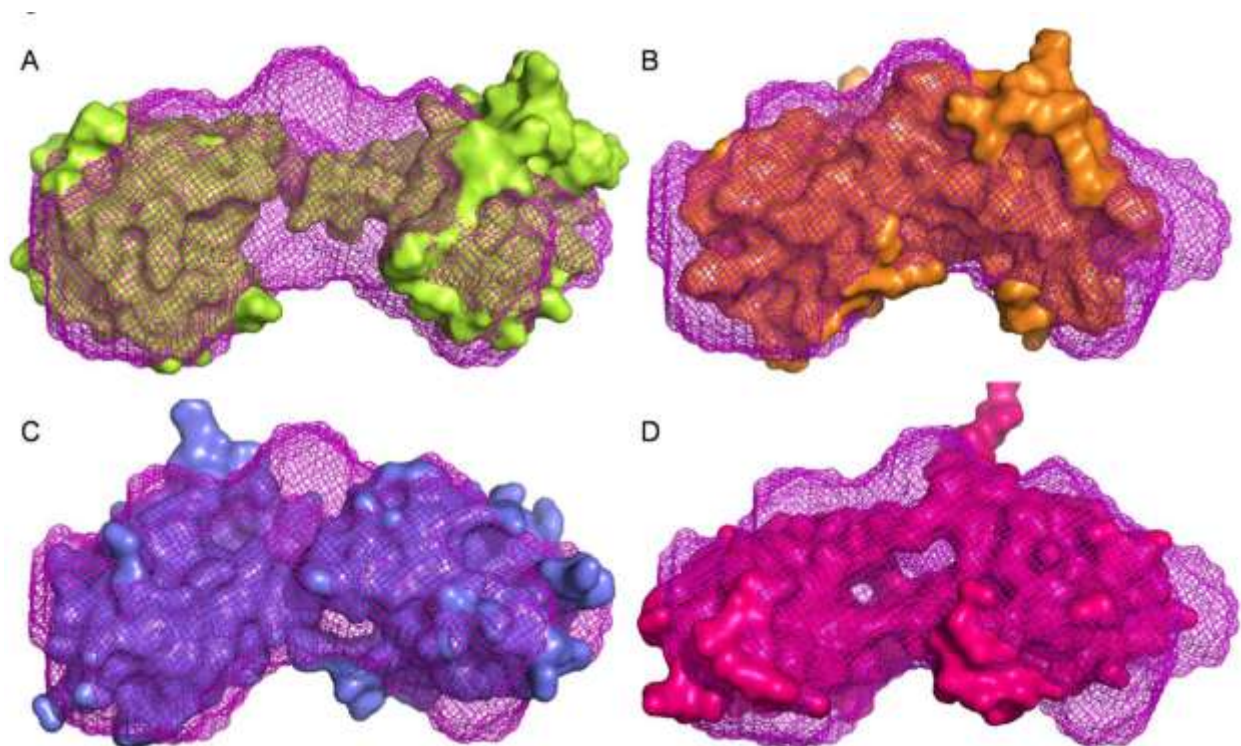
Fig. S2. Comparison of our SAXS *ab initio* model of *O*-dimer bound PSD-95 PDZ1-2 (mesh representation, magenta) with four alternative PDZ1-2 structures and models. (*A*) Surface representation of the monomeric ligand-bound NMR structure (molecule A from PDB 2KA9) (16) in green, superimposed on the SAXS model. It is seen that the domain-domain distance in the dimeric ligand-bound SAXS model is shorter than in the NMR structure. (*B*) Dimeric ligand has been docked into the apo NMR model (17) of PDZ1-2 and energy minimized (2), as here shown as an orange surface representation, and superimposed on the SAXS model. Clearly, the domain-domain orientation is more compact in the modeled NMR structure than in the solution SAXS structure. (*C*) Surface representation of the apo crystal structure presented in this manuscript (PDB 3ZRT) (blue), superimposed on the SAXS model. The overall domain-domain distance in the SAXS model is in accordance with the apo crystal structure, but their respective ligand binding sites are pointing in opposite directions. Hence the crystal structure does not represent the ligand-bound solution structure. (*D*) Surface representation (magenta red) of the apo crystal structure (PDB 3GSL) of PDZ1-2 modified in the C-terminal tail (35), superimposed on the SAXS model. Evidently the domain-domain orientation in the dimeric ligand-bound SAXS model is much different from this crystal structure.
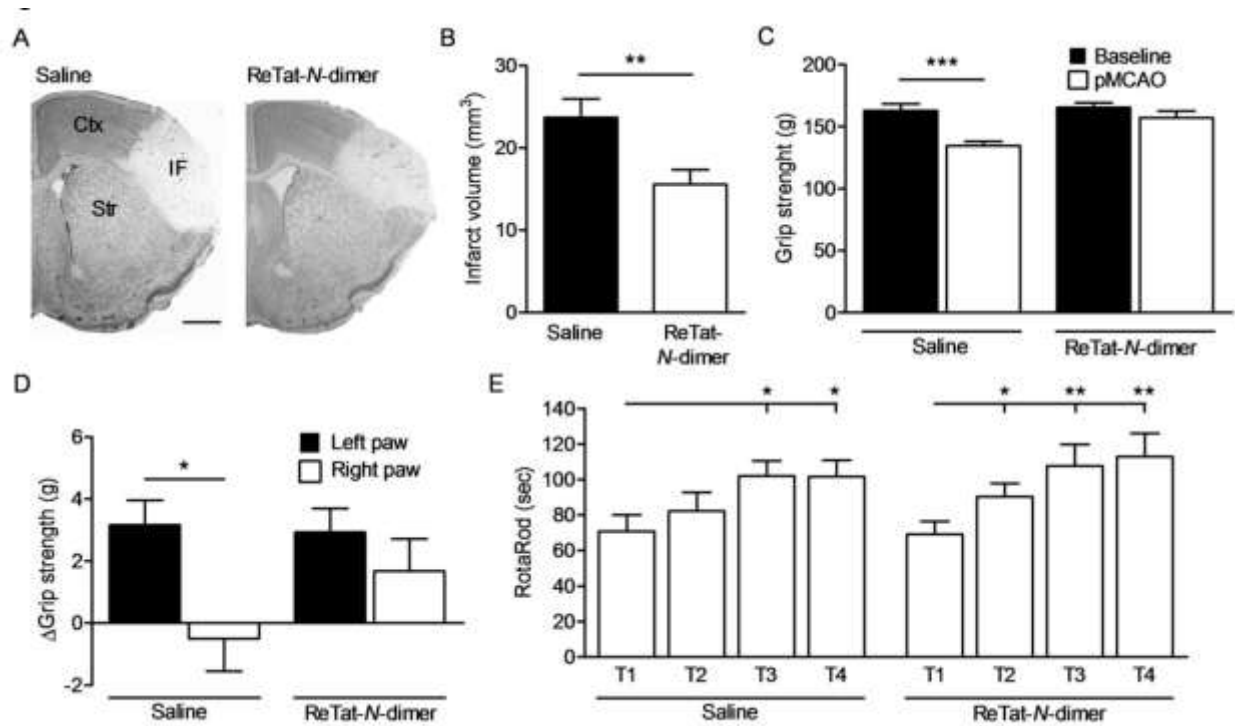
Fig. S3. Neuroprotection of ReTat-*N*-dimer, 48 hours after pMCAO in mice. (*A*) Toluidine blue staining showing the ischemic brain damage. IF: Infarct; Ctx: Cortex; Str: Striatum. Scale bar: 1mm. (*B*) Measurement of cortical infarct volumes showed that ReTat-*N*-dimer-treated mice (N = 19) developed significantly smaller infarcts (34%) compared to saline mice (N = 16). (*C-E*) Motor function assessment following pMCAO. (*C*) The total grip strength was similar before (baseline) and after pMCAO (48 h) in mice treated with ReTat-*N*-dimer (p = 0.064) compared to saline-treated mice, which showed a significant weakening in total grip strength (p<0.0001). (*D*) Grip strength analysis of the front paws showed a significant pMCAO-induced asymmetry in saline-treated mice (p = 0.014) compared to ReTat-*N*-dimer-treated mice (p = 0.22), which still showed symmetry, 48 hours after pMCAO. (*E*) Rotarod performance test over four trials (T1-T4). Treatment with ReTat-*N*-dimer gave a more pronounced (cf. T2) short-term learning skill improvement compared to saline. (*B-E*) Data are presented as mean ± SEM; */**/***: p<0.05/0.01/0.001; (*B*) Nonparametric Mann-Whitney test; (*C-D*) Paired Student's *t* test; (*E*) Wilcoxon matched pairs test.
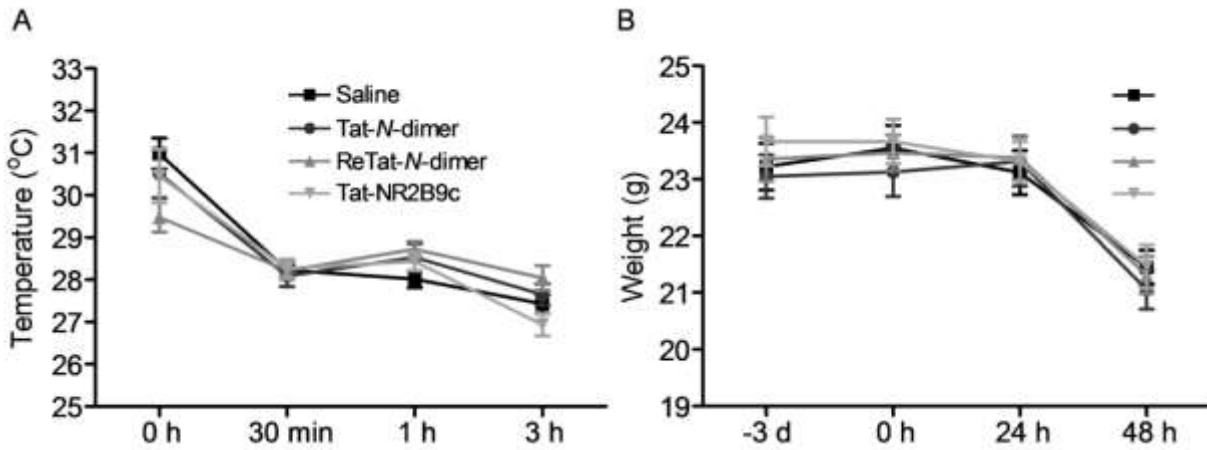
Fig. S4. Physiological parameters such as (*A*) temperature and (*B*) body weight were registered prior to and after pMCAO. Time points (x-axis) indicate time relative to surgery (0 h). (*A*) Graph showing an anesthesia-induced drop in body temperature, 30 min after pMCAO, which however was registered prior to compound administration. No compound-induced differences were registered among groups 1 and 3 hours after surgery. (*B*) Graph showing no difference in body weight among groups, 3 days prior to and 24 hours and 48 hours after pMCAO (0 h). Data shown as mean ± SEM. (*A*-*B*) Two-way Anova.

Table S1

	PSD95-PDZ1-2 (PDB 3ZRT)
Crystal data	
Space group	$P4_12_12$
Unit cell parameters	
$a = b$ (Å)	112.15
c (Å)	196.13
$\alpha = \beta = \gamma$ (°)	90.0
Mosaicity (°)	0.47-0.52
Molecules/domains in a.u.[a]	4/8
Data collection	
Resolution range (Å)	$50.16 - 3.40 \ (3.58 - 3.40)$[b]
Unique reflections	16,900
Average redundancy	3.6 (3.6)
Completeness (%)	95.4 (96.5)
R_{merge} (%)	15.9 (40.9)
I/σ(I)	4.3 (1.6)
Refinement	
Resolution range (Å)	$48.68 - 3.40 \ (3.61 - 3.40)$
Non-hydrogen atoms	5311
Built amino acid residues (overall/A/B/C/D)[c]	704/197/198/188/121
Unmodeled residues (overall/A/B/C/D)	92/2/1/11/78
R_{work} (%)[d]	21.9 (27.1)
R_{free} (%)[e]	26.4 (31.5)
Rms[f] deviation bond lengths (Å)	0.007
Rms deviation angles (°)	0.99
Ramachandran outliers (%)[g]	4.1
Average B-factor values (Å^2) (overall)	47
(A1/A2/B1/B2/C1/C2/D1/D2)[h]	40/29/41/47/56/43/107/57
Wilson B-factor (Å^2) (overall)	49

a. Asymmetric unit of the crystal.
b. Values in parentheses correspond to the outermost resolution shell.
c. A, B, C and D correspond to the four molecules located in the asymmetric unit.
d. $R_{work} = \Sigma_{hkl}(\||F_{o,hkl}| - |F_{c,hkl}\||)/|F_{o,hkl}|$, where $|F_{o,hkl}|$ and $|F_{c,hkl}|$ are the observed and calculated structure factor amplitudes.
e. R_{free} is equivalent to R_{work}, but calculated with reflections omitted from the refinement process (5 % of reflections omitted).
f. Rms = root mean square.
g. Ramachandran outliers were calculated according to Kleywegt and Jones (36)
h. Domains are divided between Ala97 and Glu98. A1, B1, C1 and D1 correspond to PDZ1 of molecules A, B, C and D, respectively. A2, B2, C2 and D2 correspond to PDZ2 of molecules A, B, C and D, respectively.

Table S2. ^{15}N R_1 and R_2 relaxation rates and {^{1}H}-^{15}N NOE measured for [^{15}N]-PSD-95 PDZ1-2 in complex with *O*-dimer (left) and unbound [^{15}N]-PSD-95 PDZ1-2 (right). Only results for residues where the assignments could be transferred with confidence from Wang et al. (16) (PDZ1-2 + *O*-dimer) or from Long et al. (17) (unbound PDZ1-2) are shown. From the R_2/R_1 ratio for a subset of the residues we extracted correlation times for molecular tumbling of 14.6 and 13.6 ns for PDZ1 and PDZ2, respectively, in PDZ1-2 in complex with *O*-dimer; and 18.3 and 18.2 ns for PDZ1 and PDZ2, respectively, in unbound PDZ1-2. This is to be compared with 14.4 and 12.5 ns in the study of PDZ1-2 and monomeric ligand by Wang et al. (16).

[^{15}N]-PSD-95 PDZ1-2 + *O*-dimer				Unbound [^{15}N]-PSD-95 PDZ1-2			
Residue	R_1 (s^{-1})	R_2 (s^{-1})	NOE	Residue	R_1 (s^{-1})	R_2 (s^{-1})	NOE
I6	1.10 ± 0.02	15.0 ± 0.4	0.56 ± 0.02	T7	0.81 ± 0.06	23.9 ± 0.8	0.54 ± 0.01
T7	0.95 ± 0.03	15.2 ± 0.6	0.70 ± 0.08	L8	0.93 ± 0.03	19.9 ± 0.9	0.76 ± 0.00
G11	1.60 ± 0.49	15.4 ± 0.6	0.50 ± 0.01	R10	0.94 ± 0.02	23.1 ± 0.6	0.69 ± 0.01
G14	0.98 ± 0.05	13.3 ± 0.8	0.45 ± 0.01	G14	0.80 ± 0.11	20.5 ± 0.6	0.62 ± 0.09
G16	1.01 ± 0.03	16.8 ± 0.8	0.83 ± 0.02	G21	0.88 ± 0.02	20.9 ± 0.4	0.75 ± 0.00
F17	1.03 ± 0.02	19.7 ± 0.6	0.66 ± 0.06	T23	0.88 ± 0.03	23.4 ± 0.7	0.59 ± 0.03
T23	0.98 ± 0.02	18.7 ± 0.7	0.80 ± 0.00	D24	0.99 ± 0.02	25.2 ± 1.4	0.81 ± 0.02
D24	1.08 ± 0.04	18.7 ± 0.7	0.83 ± 0.01	D31	1.02 ± 0.03	23.4 ± 0.3	0.51 ± 0.02
N25	1.06 ± 0.03	17.0 ± 0.7	0.65 ± 0.01	S33	0.84 ± 0.01	24.8 ± 0.4	0.72 ± 0.01
H27	1.12 ± 0.04	17.6 ± 0.9	0.76 ± 0.01	I36	0.87 ± 0.03	26.9 ± 0.7	0.81 ± 0.05
S33	1.05 ± 0.04	21.3 ± 0.9	0.82 ± 0.07	I39	0.89 ± 0.02	24.0 ± 0.3	0.68 ± 0.01
I34	1.13 ± 0.05	16.8 ± 1.2	0.90 ± 0.06	I40	0.93 ± 0.03	25.0 ± 0.6	0.71 ± 0.01
I40	1.08 ± 0.03	15.5 ± 0.9	0.85 ± 0.02	G42	0.73 ± 0.18	25.7 ± 2.6	0.76 ± 0.02
G42	0.96 ± 0.04	14.2 ± 1.3	0.68 ± 0.07	G43	0.86 ± 0.03	23.3 ± 0.5	0.69 ± 0.01
G43	0.99 ± 0.02	19.2 ± 0.8	0.77 ± 0.02	A46	0.83 ± 0.03	26.6 ± 0.5	0.80 ± 0.03
A46	1.05 ± 0.02	19.0 ± 0.6	0.80 ± 0.04	D48	0.91 ± 0.02	25.0 ± 0.7	0.67 ± 0.01
Q47	0.88 ± 0.03	17.1 ± 0.4	0.84 ± 0.00	G49	0.83 ± 0.02	24.4 ± 0.7	0.74 ± 0.06
G49	1.07 ± 0.03	16.7 ± 0.8	0.86 ± 0.02	L51	0.86 ± 0.03	25.4 ± 0.8	0.78 ± 0.04
R50	1.03 ± 0.01	18.1 ± 0.4	0.82 ± 0.03	R52	0.99 ± 0.05	25.2 ± 0.9	0.71 ± 0.02
L51	1.02 ± 0.05	18.3 ± 0.7	0.68 ± 0.00	N54	0.80 ± 0.02	28.6 ± 0.9	0.73 ± 0.02
L58	1.16 ± 0.04	16.0 ± 1.1	0.84 ± 0.02	S56	0.92 ± 0.04	25.4 ± 1.0	0.63 ± 0.02
N61	1.07 ± 0.03	25.9 ± 0.9	0.62 ± 0.01	I57	1.00 ± 0.08	23.4 ± 0.9	0.70 ± 0.06
D64	1.01 ± 0.02	17.2 ± 0.6	0.87 ± 0.05	L58	1.13 ± 0.04	25.0 ± 1.7	0.80 ± 0.15

V65	1.07 ± 0.02	16.1 ± 0.5	0.76 ± 0.02	N61	1.11 ± 0.08	29.6 ± 2.3	0.99 ± 0.00
E67	1.02 ± 0.01	16.1 ± 0.4	0.75 ± 0.02	D64	0.88 ± 0.02	22.5 ± 2.2	1.02 ± 0.03
V68	1.04 ± 0.04	17.4 ± 0.6	0.77 ± 0.00	E67	0.93 ± 0.02	23.6 ± 0.2	0.70 ± 0.00
T69	0.95 ± 0.02	17.0 ± 0.4	0.92 ± 0.03	V68	0.84 ± 0.04	28.1 ± 0.5	0.64 ± 0.00
H70	1.07 ± 0.05	15.5 ± 1.0	0.56 ± 0.12	T69	0.88 ± 0.03	24.4 ± 0.5	0.81 ± 0.04
S71	1.06 ± 0.02	16.2 ± 0.5	0.80 ± 0.03	H70	0.93 ± 0.03	22.1 ± 0.5	0.82 ± 0.00
A72	1.10 ± 0.02	18.9 ± 0.7	0.77 ± 0.04	S71	0.93 ± 0.02	22.1 ± 0.2	0.76 ± 0.01
A73	1.12 ± 0.03	17.3 ± 0.6	0.76 ± 0.07	A72	0.96 ± 0.02	26.0 ± 0.4	0.82 ± 0.04
V74	1.07 ± 0.02	15.1 ± 0.5	0.65 ± 0.02	A73	0.95 ± 0.02	25.2 ± 0.4	0.85 ± 0.07
L77	1.01 ± 0.03	15.8 ± 0.5	0.73 ± 0.03	L77	0.96 ± 0.01	22.4 ± 0.4	0.69 ± 0.02
E79	1.01 ± 0.02	16.2 ± 0.7	0.69 ± 0.05	E79	0.91 ± 0.02	23.6 ± 0.3	0.79 ± 0.05
A80	1.02 ± 0.01	18.0 ± 0.4	0.57 ± 0.01	A80	0.88 ± 0.02	23.5 ± 0.2	0.65 ± 0.03
G81	1.13 ± 0.03	16.0 ± 1.1	0.68 ± 0.00	G81	1.01 ± 0.02	21.8 ± 0.5	0.67 ± 0.02
I83	1.04 ± 0.02	16.6 ± 0.6	0.72 ± 0.02	S82	0.97 ± 0.02	21.4 ± 0.4	0.77 ± 0.01
V84	1.08 ± 0.02	15.9 ± 0.6	0.71 ± 0.01	I83	0.86 ± 0.02	23.7 ± 0.3	0.66 ± 0.02
R85	1.02 ± 0.03	19.7 ± 1.0	0.88 ± 0.04	V84	0.93 ± 0.02	23.5 ± 0.4	0.68 ± 0.02
L86	1.17 ± 0.03	15.9 ± 0.7	0.64 ± 0.07	R85	1.01 ± 0.09	28.8 ± 2.5	0.61 ± 0.11
M99	1.23 ± 0.04	16.0 ± 1.2	0.57 ± 0.01	L86	0.93 ± 0.03	21.7 ± 0.7	0.71 ± 0.03
K102	1.05 ± 0.03	13.5 ± 0.7	0.74 ± 0.02	Y87	0.92 ± 0.02	23.9 ± 0.3	0.77 ± 0.00
I104	1.09 ± 0.02	13.8 ± 0.3	0.61 ± 0.03	M89	0.78 ± 0.16	25.8 ± 1.0	0.92 ± 0.03
K105	1.23 ± 0.02	14.2 ± 0.5	0.69 ± 0.03	E96	0.95 ± 0.02	17.3 ± 0.2	0.43 ± 0.01
G106	1.05 ± 0.03	14.6 ± 0.7	0.60 ± 0.01	V98	0.95 ± 0.03	21.1 ± 0.7	0.51 ± 0.00
G109	0.99 ± 0.02	15.3 ± 0.5	0.47 ± 0.01	K102	0.93 ± 0.04	23.4 ± 0.7	0.67 ± 0.01
G111	1.18 ± 0.02	15.9 ± 0.6	0.81 ± 0.01	L103	1.06 ± 0.03	25.4 ± 0.7	0.81 ± 0.00
F112	1.18 ± 0.01	15.6 ± 0.6	0.88 ± 0.01	K105	1.03 ± 0.03	23.8 ± 0.4	0.78 ± 0.06

27

G119	1.11 ± 0.04	16.5 ± 0.9	0.87 ± 0.07	G109	1.02 ± 0.03	22.4 ± 0.6	0.61 ± 0.01
Q121	1.09 ± 0.03	15.8 ± 0.7	0.85 ± 0.03	G117	0.71 ± 0.02	23.4 ± 1.3	0.52 ± 0.00
H122	1.04 ± 0.03	17.6 ± 0.5	0.73 ± 0.02	S128	0.84 ± 0.05	28.6 ± 1.6	0.71 ± 0.00
I123	1.05 ± 0.05	12.8 ± 1.5	0.64 ± 0.09	I134	1.03 ± 0.03	21.8 ± 0.8	0.68 ± 0.01
G125	1.11 ± 0.06	12.9 ± 0.5	0.70 ± 0.09	G137	0.88 ± 0.11	26.8 ± 1.0	0.82 ± 0.00
N127	1.12 ± 0.03	15.8 ± 1.6	0.64 ± 0.01	G138	0.91 ± 0.04	24.7 ± 0.5	0.76 ± 0.03
S128	1.00 ± 0.03	19.1 ± 0.6	0.75 ± 0.01	H141	1.00 ± 0.04	25.8 ± 0.8	0.78 ± 0.01
I135	1.18 ± 0.03	15.4 ± 0.8	0.69 ± 0.03	D143	0.92 ± 0.03	23.4 ± 0.4	0.77 ± 0.03
E136	1.12 ± 0.06	18.7 ± 1.0	0.72 ± 0.04	G144	0.82 ± 0.03	22.1 ± 0.9	0.81 ± 0.01
G137	1.06 ± 0.05	13.9 ± 1.2	1.27 ± 0.14	I148	0.89 ± 0.02	26.1 ± 0.4	0.75 ± 0.00
G138	1.06 ± 0.03	17.3 ± 0.6	0.67 ± 0.02	G149	0.97 ± 0.05	25.9 ± 0.8	0.77 ± 0.02
H141	1.27 ± 0.04	17.0 ± 1.4	0.69 ± 0.02	D150	0.94 ± 0.02	27.2 ± 0.5	0.82 ± 0.02
K142	1.11 ± 0.04	13.5 ± 0.7	0.71 ± 0.01	L153	1.01 ± 0.04	24.4 ± 0.7	0.76 ± 0.03
D143	1.16 ± 0.02	14.4 ± 0.5	0.90 ± 0.02	N156	1.02 ± 0.02	24.1 ± 0.4	0.74 ± 0.00
G144	1.02 ± 0.02	14.5 ± 1.2	0.82 ± 0.00	V158	1.05 ± 0.02	23.5 ± 0.5	0.73 ± 0.03
I148	1.11 ± 0.03	16.1 ± 0.4	0.70 ± 0.04	D162	1.06 ± 0.04	23.7 ± 0.5	0.79 ± 0.01
G149	1.10 ± 0.03	18.2 ± 0.8	0.74 ± 0.03	M164	0.99 ± 0.02	26.5 ± 1.0	0.90 ± 0.01
D150	1.15 ± 0.02	18.1 ± 0.5	0.81 ± 0.02	D167	0.91 ± 0.01	22.8 ± 0.2	0.69 ± 0.02
L153	1.12 ± 0.03	15.3 ± 0.9	0.76 ± 0.00	A168	0.95 ± 0.02	26.3 ± 0.4	0.71 ± 0.01
V155	1.14 ± 0.04	16.7 ± 0.5	0.68 ± 0.01	V179	1.02 ± 0.02	23.4 ± 0.5	0.65 ± 0.02
N156	1.19 ± 0.03	17.0 ± 0.7	0.76 ± 0.09	K182	1.25 ± 0.12	16.8 ± 1.4	0.21 ± 0.00
E166	1.03 ± 0.02	17.8 ± 0.5	0.74 ± 0.06	V183	1.02 ± 0.03	26.5 ± 0.7	0.82 ± 0.01
A168	1.00 ± 0.02	18.0 ± 0.4	0.71 ± 0.01	A184	0.92 ± 0.02	25.5 ± 0.7	0.67 ± 0.05
V169	1.02 ± 0.02	19.3 ± 0.6	0.75 ± 0.10	K185	1.04 ± 0.04	27.5 ± 1.1	0.65 ± 0.00
L172	1.03 ± 0.02	16.2 ± 0.6	0.63 ± 0.03	A189	0.92 ± 0.01	2.47 ± 0.1	-0.76 ± 0.00

T175	1.05 ± 0.03	9.0 ± 0.4	0.40 ± 0.00				
V178	1.02 ± 0.02	13.2 ± 0.3	0.68 ± 0.02				
V179	1.12 ± 0.02	15.2 ± 0.7	0.71 ± 0.10				
L181	1.06 ± 0.03	15.3 ± 0.6	0.93 ± 0.04				

Table S3. Overall parameters determined from SAXS data. Samples were measured in the concentration range 0.25–7.1 mg/ml except for O-dimer samples, where data was used only in the range 0.25–4 mg/ml. PDZ1-2:ligand ratio was 1:5 for both IETAV and O-dimer at all protein concentrations. Oligomeric range is determined from the molecular mass, which is proportional to the scattering extrapolated to zero angles. Radius of gyration (R_g) and D_{max} values are extracted from the fourier transform of the background-subtracted data. Radius of gyration was also calculated using the guinier approximation, yielding identical values. Typical distances are interpreted as the distance between center of masses of the individual PDZ domains. All values are in nm, except for the unit-less oligomeric range. The apo PDZ1-2 protein shows a concentration-dependent dimerization in solution, as also observed for other PDZ domains (37), whereas complete monomerization was seen upon addition of the ligands.

Sample	Oligomeric range	R_g (nm)	D_{max} (nm)	Typical distance (nm)
Apo	1.3-1.9	2.7	10.0	3.3
IETAV	1.0-1.3	2.4	7.9	3.9
O-dimer	1.0-1.1	2.2	7.0	3.6

Table S4. Blood values monitored during the pMCAO (48 hour survival period) experiment at 1 hour after surgery. Values are shown as mean ± SEM. ´Control´ indicates non-manipulated animals.

Value	Control	Saline	Tat-N-dimer	ReTat-N-dimer	Tat-NR2B9c
pH	7.19 ± 0.03	7.17 ± 0.01	7.16 ± 0.01	7.13 ± 0.01	7.13 ± 0.01
pCO_2 (mmHg)	88.4 ± 2.7	101 ± 2.7	95.7 ± 2.3	104 ± 2.5	106 ± 2.4
pO_2 (mmHg)	47.6 ± 3.4	54.0 ± 1.6	50.2 ± 2.2	56.4 ± 2.9	55.2 ± 2.6
$[Na^+]$ (mmol/L)	145 ± 0.3	147 ± 0.6	148 ± 2.0	147 ± 0.5	147 ± 0.3
$[K^+]$ (mmol/L)	5.6 ± 0.21	4.8 ± 0.09	5.2 ± 0.20	5.1 ± 0.18	5.1 ± 0.13
$[Ca^{2+}]$ (mmol/L)	1.29 ± 0.01	1.32 ± 0.01	1.30 ± 0.02	1.31 ± 0.01	1.32 ± 0.01
[Glucose] (mmol/L)	139 ± 4.5	146 ± 6.2	134 ± 7.9	154 ± 8.1	141 ± 7.4
[Lactate] (mmol/L)	0.99 ± 0.04	0.90 ± 0.06	0.93 ± 0.07	0.90 ± 0.05	0.87 ± 0.07
Hct (%)	42.8 ± 0.4	42.0 ± 0.5	43.5 ± 0.9	41.3 ± 0.6	40.8 ± 0.6